R. Vescovini, E. Spigarolo, E.L. Jansen, L. Dozio
Efficient Post-Buckling Analysis of Variable-Stiffness Plates Using a Perturbation Approach
Thin-Walled Structures, Vol. 143, 2019, 106211 (16 pages)
doi:10.1016/j.tws.2019.106211

Efficient Post-Buckling Analysis of Variable-Stiffness Plates Using a Perturbation Approach

R. Vescovini[1,*], E. Spigarolo[1], E. Jansen[2], L. Dozio[1]

[1] *Dipartimento di Scienze e Tecnologie Aerospaziali, Politecnico di Milano*

Via La Masa 34, 20156 Milano, Italy

[2] *Institut fur Statik und Dynamik, Leibniz Universitat Hannover*

Appelstrasse 9A 30167 Hannover, Germany

Abstract

The present work discusses the development of a formulation for efficiently analyzing variable-stiffness plates operating in the post-buckling regime. The approach relies upon the combined use of a single-mode Koiter's perturbation strategy along with a mixed variational formulation expressed in terms of Airy stress function and out-of-plane displacement, where the unknowns are approximated using global trial functions based on Legendre polynomials. A highly efficient numerical tool is achieved, which allows to analyze the initial post-buckling field with the ease of closed-form solution, but a much wider field of employ in terms of elastic couplings, boundary and loading conditions. The quality of the predictions is illustrated by means of a comprehensive set of comparisons against results from the literature. Possible applications of the approach are shown, where the exploration of the design space offered by curvilinear fibers requires thousands of non-linear post-buckling analyses to be run.

Keywords: Post-buckling; variable-stiffness; perturbation approach; reduced-order models.

1 Introduction

The variable-stiffness (VS) concept relies upon the idea of allowing fibers to run along non-straight paths, such that elastic tailoring can be pursued with improved design flexibility with respect to classical, straight-fiber composites. This idea has attracted the interest of many researchers in the past years, as improved mechanical performances can be achieved and more efficient structures obtained.

Early studies on variable-stiffness structures date back to almost 50 year ago [1], however the lack of available technologies hindered the progress of this concept until the early nineties, when renewed interest was raised

*Corresponding author. *Email address:* riccardo.vescovini@polimi.it (Riccardo Vescovini)

thanks to the works of Leissa and Martin [2], Hyer and Charette [3, 4] and Gürdal and Olmedo [5].
In the past years, recent improvements of manufacturing techniques further promoted the variable-stiffness concept as a suitable candidate for the aerostructures of the next generation.
The advantages offered by VS designs regard a wide range of structural responses, and the tailoring opportunities can be exploited to obtain improved behaviour in terms of buckling loads [4, 6–8], critical temperatures [9, 10], fundamental frequencies [11–14] and failure loads [15, 16]. The bending response of VS doubly-curved shells and plates was assessed in [17, 18]. Variable-stiffness plates were also proposed in the context of morphing applications were multiple-stable shapes are used for allowing change of configuration [19–21].
Among the above mentioned opportunities, the elastic stability is one of the primary concern in the design of thin panels commonly employed in aerospace applications. Indeed, the relatively small thicknesses along with typical loading conditions that may promote instability render buckling and post-buckling analyses a crucial aspect during the design phase. Accordingly, the availability of adequate numerical tools, capable of combining computational efficiency and accuracy of the predictions, is a necessary aspect to properly exploit the potentialities offered by VS panels.
The buckling response is addressed referring to finite element simulations in Refs. [22, 23], where design optimization are performed using lamination parameters. One side effect of the improved design flexibility offered by VS designs is the exponentially increasing number of design parameters. For this reason, finite element simulations can be too costly, and alternative and less expensive analyses strategies can be helpful for reducing the overall design procedure phase. Metamodels were proposed as a mean for speeding-up the optimization phase of VS cylinders in [24]. The robustness and the good convergence properties of the Differential Quadrature Method (DQM) motivated its use for addressing pre-buckling, buckling and post-buckling behaviour of VS plates [25, 26]. Another approach recently proposed in this field regards the application of the isogeometric analysis (IGA) for analysis and design optimization of variable-stiffness plates [27, 28].
The method of Ritz is another well-known strategy for guaranteeing fast yet accurate predictions, especially when relatively simple geometries are of concern. In this context, the linear buckling behaviour of VS plates is addressed in Refs. [8, 9, 29–32].
The availability of computationally effective tools is even more important when the post-critical response is of concern, and non-linear simulations need to be conducted. The effectiveness of a Ritz-like implementation was demonstrated by Wu et. al that developed a non-linear approach based on a mixed variational approach [33], successfully applied in the context of design optimizations including post-buckling requirements [34, 35].
Plate assembly models were proposed for assessing the mechanical and thermal post-buckling behaviour of stiffened plates in Refs. [36, 37], using a displacement-based approach along with a Ritz solution technique.
An alternative way of achieving computational efficiency consists in making use of reduced-order models, based on the well-known perturbation approach due to Koiter [38]. This approach was pursued by Rahman et al. [39, 40] that developed a shell finite element in the DIANA code, demonstrating its use in the context

of VS plate analysis. A finite element-based implementation of Koiter's asymptotic theory has been recently proposed by Madeo et al. [41] and applied to the post-buckling analysis of axially compressed VS plates was addressed, illustrating the importance of multi-modal expansions for long plates. Still in the context of finite element-based approaches, an application of the Koiter-Newton approach to variable-stiffness plates is available in [42]. The potentialities offered by the Koiter's approach to real-life structures such as frames, channel sections and wing-boxes can be found in [43, 44].

An interesting approach to further reduce the computational time for the post-buckling analysis consists in combining the Koiter's asymptotic approach with efficient mesh-free techniques. Recently, White et al. [45] introduced this idea by coupling Koiter's theory and differential quadrature (GDQ) and integral quadrature (GIQ) approaches for the initial post-buckling analysis of curved panels. Koiter's approach was used in conjunction with generalized differential-integral quadrature method in Ref. [46]. Due to reduced computational costs, the approach was successfully applied to minimize post-buckling loss of stiffness, illustrating the superiority offered by VS configurations [47].

Starting from this latest idea, the present work aims at presenting a formulation for the initial post-buckling analysis of variable-stiffness panels that allows to further reduce the time for the analysis. The model stems from a combined use of Koiter's perturbation method along with a mixed variational approach – previously applied to composite panels [48, 49] and to variable-stiffness plates [33–35] –, which is applied referring to a Ritz solution strategy. The present investigation is not primarily aimed at presenting the advantages due to variable-stiffness designs – they have been already established by past research efforts –, but rather at illustrating a highly efficient computational tool that can be successfully used for assessing the initial post-buckling response. Specifically, the work discusses a tool whose efficiency is comparable to closed-form solutions, while removing typical restrictions in terms of fields of employ. At the same time, the method inherits the advantages of semi-analytical approaches, where wide range of configurations can be handled in terms of elastic couplings, boundary and loading conditions. The accuracy of the predictions is demonstrated by comparison against benchmarks from the literature, while design charts are presented for selected VS configurations to show a potential use of the proposed approach.

2 Formulation

The formulation is developed for the analysis of thin plates obtained by the stacking of plies with non-uniform stiffness properties. It is assumed that the laminate is symmetric and balanced, meaning that in-plane and out-of- plane coupling effects are absent, as well as those due to shear-extension coupling.

A sketch of the plate is provided in Figure 1. The reference surface of the plate is taken in correspondence of the midsurface, and an orthogonal reference system xyz is considered. The origin is taken at the middle of the plate. The thickness is denoted with h, whilst l_x and l_y are the planar dimensions along the x and

y directions, respectively. Note that the common nomenclature a and b is not adopted here to avoid any confusion with the post-buckling coefficients introduced next. The load is applied in the form of a prescribed axial shortening of total magnitude $\overline{u}$ taken positive in compression. It can be noted that this condition determines a non-uniform edge-wise stress distribution even in the linear pre-buckling field.

It assumed that the plate is free to expand or contract along the transverse direction, so the in-plane boundary conditions are:

$$\begin{cases} N_{xy} = 0 & \text{on} \quad \partial S \\ N_{yy} = 0 & \text{on} \quad y = \pm l_y/2 \\ u = \overline{u}/2 & \text{on} \quad x = \pm l_x/2 \end{cases} \tag{1}$$

where $S \equiv [-l_x/2, l_x/2] \times [-l_y/2, l_y/2]$, and ∂S denotes the plate boundaries.

Other common in-plane boundary conditions are those of transverse edges prevented from expansion or free to expand, while remaining straight. Those cases, as well as that of prescribed edge forces, can be handled by modifying the formulation as discussed by Wu et al. [33]. Regarding the flexural boundary conditions, the edges can be subjected to any combination of free (F), simply-supported (S) and clamped conditions (C). According to notation adopted hereinafter, the conditions are specified by using a letter for each edge, starting from the one at $x = -l_x/2$, and moving along the counter-clockwise direction.

The kinematic model is based upon von Kármán large deflection theory, which provides the membrane strain-displacement relation in the form:

$$\epsilon_{xx} = u_{,x} + \frac{1}{2} w_{,x}^2 \qquad \epsilon_{yy} = v_{,y} + \frac{1}{2} w_{,y}^2 \qquad \gamma_{xy} = u_{,x} + v_{,y} + w_{,x} w_{,y} \tag{2}$$

where the comma followed by an index denotes differentiation with respect to that index, and u, v and w are the three displacement components of the reference surface along the directions x, y and z, respectively. According to von Kármán theory, the effects of geometric non-linearity are due to the out-of-plane displacements w, whereas the quadratic contributions associated with the displacement components u and v are assumed negligible.

The plate curvatures are obtained as:

$$k_{xx} = -w_{,xx} \qquad k_{yy} = -w_{,yy} \qquad k_{xy} = -2w_{,xy} \tag{3}$$

The von Kármán kinematic model has been traditionally used in the framework of semi-analytical models to analyze the buckling and post-buckling behaviour of plate-type structures. It has been pointed out in the context of the Finite Element implementation of Koiter's approach [50, 51], that the von Kármán model involves certain kinematic issues which require specific care when analyzing the behaviour of structures through this perturbation approach. These previous studies have also shown, that these kinematic issues do not have a severe effect on the accuracy of the results, when the post-buckling field is characterized by strong stress redistributions.

The plate constitutive relation, expressed in its semi-inverse form, and according the hypothesis of symmetric and balanced laminate, reads:

$$\begin{Bmatrix} \boldsymbol{\epsilon} \\ \mathbf{M} \end{Bmatrix} = \begin{bmatrix} \mathbf{a}(x,y) & \mathbf{0} \\ \mathbf{0} & \mathbf{D}(x,y) \end{bmatrix} \begin{Bmatrix} \mathbf{N} \\ \mathbf{k} \end{Bmatrix} \tag{4}$$

The matrix $\mathbf{a}$ collects the coefficients of the laminate membrane compliance, i.e. $\mathbf{a} = \mathbf{A}^{-1}$ where $\mathbf{A}$ is the membrane stiffness according to the Classical Lamination Theory (CLT) and, similarly, $\mathbf{D}$ defines the bending stiffness matrix. The vectors $\boldsymbol{\epsilon}$ and $\mathbf{k}$ collect the strain and curvature components according to Eqs. (2) and (3), while $\mathbf{N}$ and $\mathbf{M}$ are the membrane forces and moments per unit length [52, 53].

The expression of Eq. (4) accounts for the dependence of the elasticity coefficients on the position x, y over the plate domain, and provides a relation of general validity for the case of variable stiffness panels. The present study focuses on panels characterized by a linear variation of the fiber angle, according to sketch reported in Figure 2.

Specifically, the laminate is obtained as a stack of plies with fiber angles varying linearly with respect to a local reference system $x'y'$, generically rotated by an angle Φ with respect to the global system xy. The fiber angle, measured with respect to the reference $x'y'$ and taken positive for counter-clockwise rotations with respect to the axis $z = z'$, is equal to T_0 at the center of the plate, and T_1 at a distance d from the center along the direction x' [8, 29]. According to this assumption, each ply is specified by $[\Phi < T_0 | T_1 >]$, and the orientation is given by:

$$\theta(x,y) = \theta(x') = \Phi + (T_1 - T_0)\frac{x'}{d} + T_0 \tag{5}$$

It is remarked that the fiber orientation depends on both x and y, thus the formulation is developed with sufficient generality for handling any constitutive law with elastic coefficients varying from point to point. Due to its simplicity and the possibility of highlighting the plate response with relatively few degrees of freedom, the description of Eq. (5) will be adopted next. In addition, the angles Φ will be restricted to the case of 0 and 90 degrees, representing a change of the fiber orientation along the x or y direction, respectively. Accordingly, the reference distances d are taken equal to l_x and l_y.

2.1 Variational principle

The formulation is developed in the context of a mixed variational approach expressed in terms of out-of-plane deflections and Airy stress function F, the latter defined as:

$$N_{,xx} = F_{,yy} \qquad N_{,yy} = F_{,xx} \qquad N_{,xy} = -F_{,xy} \tag{6}$$

The problem is thus formulated in terms of two unknown fields, instead of three as in the case of purely displacement-based approaches. This leads to a considerable advantage in terms of size of the problems to be solved when an approximate solution is sought. The definition of the Airy stress function of Eq. (6)

guarantees that in-plane equilibrium conditions are identically satisfied, whereas an additional requirement is needed for expressing the compatibility of the membrane strains. To this aim, the following functional, due to Giavotto [54, 55] and successively used by Vescovini and Bisagni [48, 49] and Wu et al. [33–35], is introduced:

$$\begin{aligned}\Pi_U = &-\frac{1}{2}\int_S \left[a_{11}(x,y)F_{,yy}^2 + 2a_{12}(x,y)F_{,xx}F_{,yy} + a_{22}(x,y)F_{,xx}^2 + a_{66}(x,y)F_{,xy}^2\right]\,\mathrm{d}S + \\ &+\frac{1}{2}\int_S \left[D_{11}(x,y)w_{,xx}^2 + 2D_{12}(x,y)w_{,xx}w_{,yy} + D_{22}(x,y)w_{,yy}^2 + \right. \\ &\left. + 4D_{66}(x,y)w_{,xy}^2 + 4D_{16}(x,y)w_{,xx}w_{,xy} + 4D_{26}(x,y)w_{,yy}w_{,xy}\right]\,\mathrm{d}S + \\ &+\frac{1}{2}\iint_S \left[F_{,yy}w_{,x}^2 + F_{,xx}w_{,y}^2 - 2F_{,xy}w_{,x}w_{,y}\right]\,\mathrm{d}S - \int_{-l_y}^{+l_y} F_{,yy}\frac{\overline{u}}{2}\bigg|_{\pm l_x}\,\mathrm{d}y\end{aligned} \tag{7}$$

It is worth noting that the adoption of a mixed-formulation is particularly effective to guarantee fast convergence of the membrane stress resultants. Furthermore, typical membrane locking phenomena occurring in displacement-based finite element approximations are avoided. Also it is observed that the extension to first-order shear deformation theory can be derived following the steps discussed in Ref. [55].

The variational principle associated with Eq. (7) states that membrane compatibility and out-of-plane equilibrium are identically satisfied by imposing the vanishing of the first variation of Π_U, i.e.:

$$\delta\Pi_U = 0 \tag{8}$$

The functional of Eq. (7) embeds the von Kármán large deflection compatibility and equilibrium equations into one single scalar expression – for this reason it will be referred hereinafter as unitary. The functional can be derived by formulating the weak form of the von Kármán equations, and applying the divergence theorem to lower the maximum order of derivation of the unknown functions w and F. In other words, and following the inverse approach, the non-linear equilibrium and compatibility equations can be obtained by application of the Euler-Lagrange equations to the functional of Eq. (7). It can be noted that the third integral accounts for geometric non-linearities as far as it is quadratic with respect to w and linear in F. The fourth integral contribution is associated with the imposed axial displacement $\overline{u}$, and is omitted whenever the load is introduced in the form of a prescribed edge force.

The non-linear functional of Eq. (7) is suitable for formulating the post-buckling problem of thin plates using direct solution strategies [33, 48, 49], such as the Ritz method. In this work, a perturbation approach is proposed in conjunction with a Ritz-like approximation of the unknown functions for the fast analysis of the initial post-buckling field.

2.2 Perturbation approach

The perturbation approach has been historically used in a number of problems in the field of elastic stability. Pioneering work is due to Koiter [38] that employed this strategy for explaining the imperfection sensitivity of

shell-like structures. The approach consists essentially in performing an asymptotic expansion in proximity of the bifurcation load to be valid in the initial post-buckling range. Based on the unknown functions entering the functional of Eq. (7), the asymptotic solution of Eq. (8) is sought in the form:

$$\begin{aligned} F &= \lambda F^{(0)} + \xi F^{(1)} + \xi^2 F^{(2)} \\ w &= \lambda w^{(0)} + \xi w^{(1)} + \xi^2 w^{(2)} \end{aligned} \tag{9}$$

where ξ is a perturbation parameter, whilst the superscripts 0,1 and 2 identify the solutions of the zero-, first- and second-order problems, respectively. Furthermore, a single-mode approximation is assumed, meaning that the behaviour in the surrounding of the bifurcation point is approximated by accounting for the buckled shape corresponding to the lowest eigenvalue. This assumption can be reasonably introduced whenever the lowest eigenvalues are well-separated, which is generally the case for plate-like structures. As demonstrated by Rahman et al. [40], clustered modes may characterize the behaviour of variable stiffness plates optimized for maximum buckling load. For the current analysis, it is assumed that no modal interaction occurs, and the analyses are conducted by considering N single-mode approximations, where N is the number of clustered modes within a given threshold. This approach leads to a simple and efficient formulation. In those cases in which an interaction between buckling modes influences the post-buckling behaviour, the use of the multi-mode expansion would be necessary.

Two possible ways can be considered for deriving the governing equations of the perturbation approach. The first one consists in substituting the expansion of Eq. (9) into Eq. (7) and, after collecting the terms pre-multiplied by corresponding powers of ξ, the partial differential equations associated with the zero-, first- and second-order problems are retrieved by imposing the variational principle of Eq. (8). The resulting set of equations can then be solved exactly or approximately using a series expansion of the unknowns. This is the strategy employed, for instance, by Arbocz et al. [56, 57], where the approach is developed starting from the strong form formulation of the problem.

A second and alternative strategy is pursued in this work. Specifically, the unknowns are firstly expanded using global functions, and the perturbation is then introduced at unknown amplitudes level. The two approaches lead to the same set of discrete equations to be solved, but this second strategy is preferred here due to the ease of derivation of the final governing equations.

Following previous works of Refs. [25, 29, 33], the Airy stress function and the out-of-plane displacements are represented with a Ritz-like expansion as:

$$F(\xi,\eta) = F_0(\eta) + F_1(\xi,\eta) = F_0(\xi) + \sum_{p=0}^{P}\sum_{q=0}^{Q} \phi_{pq} X_p(\xi) Y_q(\eta) \tag{10}$$

where the nondimensional coordinates $\eta = 2x/l_x$ and $\xi = 2y/l_y$, defined in the range $[-1, +1]$ are introduced. The stress function is divided into a contribution describing the stress resultants along the boundaries, F_0,

and inside the plate domain, F_1. These two functions, in turn, are represented as:

$$N_{x0} = F_{,yy} = \frac{4}{b^2} F_{0,\eta\eta} = \frac{4}{b^2} \sum_{k=0}^{K} c_k L_k(\eta) \tag{11}$$

and:

$$\begin{aligned} X_p(\xi) &= f(\xi) L_p(\xi) = (1-\xi^2)^2 L_p(\xi) \\ Y_q(\eta) &= f(\eta) L_q(\eta) = (1-\eta^2)^2 L_q(\eta) \end{aligned} \tag{12}$$

where the generic term L_i is the Legendre polynomial of order i, whilst the quartic boundary functions f ensure the fulfillment of the homogenous boundary conditions. The unknown amplitudes are given the terms ϕ_{pq} and c_k of Eqs. (10) and (11), respectively.
Similarly, the out-of-plane deflections are described as:

$$w(\xi,\eta) = \sum_{m=0}^{M} \sum_{n=0}^{N} w_{mn} \overline{X}_m(\xi) \overline{Y}_n(\eta) \tag{13}$$

The unknowns w_{mn} are the $(M+1) \times (N+1)$ coefficients of the series, while $\overline{X}_m(\xi)$,$\overline{Y}_n(\eta)$ are the trial functions satisfying the flexural essential boundary conditions, which are taken as:

$$\begin{aligned} \overline{X}_m(\xi) &= (1-\xi)^{i_1} (1+\xi)^{i_2} L_m(\xi) \\ \overline{Y}_n(\eta) &= (1-\eta)^{j_1} (1+\eta)^{j_2} L_n(\eta) \end{aligned} \tag{14}$$

where the indices i_k, j_k can be either 0, 1, or 2 depending on the boundary conditions, and correspond, respectively, to free, simply-supported and clamped conditions.
Following the asymptotic expansion of Eq. (9), and on the basis of the Ritz approximations given by Eqs. (10) and (13), it is possible to express the unknown amplitudes as:

$$\begin{cases} c_k = \lambda c_k^{(0)} + \xi c_k^{(1)} + \xi^2 c_k^{(2)} + \cdots \\ \phi_{pq} = \lambda \phi_{pq}^{(0)} + \xi \phi_{pq}^{(1)} + \xi^2 \phi_{pq}^{(2)} + \cdots \\ w_{mn} = \lambda w_{mn}^{(0)} + \xi w_{mn}^{(1)} + \xi^2 w_{mn}^{(2)} + \cdots \end{cases} \tag{15}$$

A formal substitution of the expansion of Eq. (15) into Eqs. (10) and (13) and then into Eq. (7) allows to approximate the unitary functional with the expansion:

$$\Pi_U = \Pi_U^{(0)} + \xi^2 \Pi_U^{(1)} + \xi^4 \Pi_U^{(2)} + \cdots \tag{16}$$

where the index in the parenthesis defines the order of the problem, which is derived after imposing the stationarity condition, i.e.:

$$\delta \Pi_U^{(k)} = \delta \mathbf{c}^{\mathrm{T}} \frac{\partial \Pi_U^{(k)}}{\partial \mathbf{c}} + \delta \mathbf{\Phi}^{\mathrm{T}} \frac{\partial \Pi_U^{(k)}}{\partial \mathbf{\Phi}} + \delta \mathbf{w}^{\mathrm{T}} \frac{\partial \Pi_U^{(k)}}{\partial \mathbf{w}} = 0 \qquad \forall \delta \mathbf{c}, \delta \mathbf{\Phi}, \delta \mathbf{w} \qquad k = 0, 1, 2 \tag{17}$$

having collected the Ritz amplitudes into the vectors $\mathbf{c}$, $\mathbf{\Phi}$ and $\mathbf{w}$.

One can observe that pre-buckling equations are available in the form of equilibrium conditions by imposing the vanishing of $\delta\Pi_U^{(0)}$; the buckling problem is obtained by setting to zero the variation of the quadratic part of the functional, i.e. $\delta\Pi_U^{(1)}$, which is, as a matter of fact, an application of the Trefftz criterion [58, 59]; the second-order problem, necessary for the assessment of the initial post-buckling response, is available from the condition $\delta\Pi_U^{(2)} = 0$.

Specifically, the zero-order problem is obtained as:

$$\begin{cases} \mathbf{S}^{cc}\mathbf{c}^{(0)} + \mathbf{S}^{c\Phi}\mathbf{\Phi}^{(0)} + \dfrac{1}{2}\mathbf{w}^{(0)\mathrm{T}}\hat{\boldsymbol{\mathcal{N}}}_k\mathbf{w}^{(0)} = \mathbf{P}^{\mathrm{c}}\lambda \\ \mathbf{S}^{\Phi c}\mathbf{c}^{(0)} + \mathbf{S}^{\Phi\Phi}\mathbf{\Phi}^{(0)} + \dfrac{1}{2}\mathbf{w}^{(0)\mathrm{T}}\boldsymbol{\mathcal{N}}_{pq}\mathbf{w}^{(0)} = \mathbf{0} \\ \mathbf{K}^{ww}\mathbf{w}^{(0)} + \mathbf{c}^{(0)\mathrm{T}}\hat{\boldsymbol{\mathcal{N}}}_{mn}\mathbf{w}^{(0)} + \mathbf{\Phi}^{(0)\mathrm{T}}\boldsymbol{\mathcal{N}}_{mn}\mathbf{w}^{(0)} = \mathbf{0} \end{cases} \tag{18}$$

where the relevant terms multiplying the unknown amplitudes are obtained from the integration of the surface integrals of the unitary functional, and are reported in the Appendix. To this aim, numerical integration is performed using Gauss quadrature.

The solution of the linear pre-buckling problem of Eq. (18), on the basis of the assumption of symmetric laminate, implies that $\mathbf{w}^{(0)} = \mathbf{0}$. The problem is then simplified to the solution of the linear system given by the first two sets of equations of Eq. (18), where the non-linear terms are identically zero. The size of the linear system is then (P+1)(Q+1), with additional K + 1 degrees of freedom if the load is introduced in the form of prescribed displacement.

The first-order problem is obtained by taking $k = 1$ into Eq. (17), and leads to the following set of equations:

$$\begin{cases} \mathbf{S}^{cc}\mathbf{c}^{(1)} + \mathbf{S}^{c\Phi}\mathbf{\Phi}^{(1)} + \dfrac{1}{2}\mathbf{w}^{(0)\mathrm{T}}\hat{\boldsymbol{\mathcal{N}}}_k\mathbf{w}^{(1)} + \dfrac{1}{2}\mathbf{w}^{(1)\mathrm{T}}\hat{\boldsymbol{\mathcal{N}}}_k\mathbf{w}^{(0)} = \mathbf{0} \\ \mathbf{S}^{\Phi c}\mathbf{c}^{(1)} + \mathbf{S}^{\Phi\Phi}\mathbf{\Phi}^{(1)} + \dfrac{1}{2}\mathbf{w}^{(0)\mathrm{T}}\boldsymbol{\mathcal{N}}_{pq}\mathbf{w}^{(1)} + \dfrac{1}{2}\mathbf{w}^{(1)\mathrm{T}}\boldsymbol{\mathcal{N}}_{pq}\mathbf{w}^{(0)} = \mathbf{0} \\ \mathbf{K}^{ww}\mathbf{w}^{(1)} + \left(\mathbf{c}^{(0)\mathrm{T}}\hat{\boldsymbol{\mathcal{N}}}_{mn} + \mathbf{\Phi}^{(0)\mathrm{T}}\boldsymbol{\mathcal{N}}_{mn}\right)\mathbf{w}^{(1)} + \left(\mathbf{c}^{(1)\mathrm{T}}\hat{\boldsymbol{\mathcal{N}}}_{mn} + \mathbf{\Phi}^{(1)\mathrm{T}}\boldsymbol{\mathcal{N}}_{mn}\right)\mathbf{w}^{(0)} = \mathbf{0} \end{cases} \tag{19}$$

where the amplitudes identified by the superscript (0) are available from the pre-buckling solution, while the unknowns are those associated with the superscript (1).

Due to the null deflections in the pre-buckling range, the in-plane and out-of-plane first-order equations are uncoupled, and the first-order solution is sought by considering the third of Eq. (19) as:

$$\left[\mathbf{K}^{ww} + \lambda\left(\mathbf{c}^{(0)\mathrm{T}}\hat{\boldsymbol{\mathcal{N}}}_{mn} + \mathbf{\Phi}^{(0)\mathrm{T}}\boldsymbol{\mathcal{N}}_{mn}\right)\right]\mathbf{w}^{(1)} = \mathbf{0} \tag{20}$$

The problem is in the form of a standard eigenvalue problem, where the buckling multiplier λ_{cr} is obtained as the lowest positive eigenvalue, whilst the shape of the buckled surface is the corresponding eigenvector. Due to the uncoupling between in-plane and out-of-plane behaviour, the total number of degrees of freedom is restricted to (P+1)(Q+1). For consistency with the formulae presented next for the post-buckling response,

the first-order modes are scaled to have unitary ratio between the maximum modal displacement and the plate thickness.

It is noted that the set of discrete equations given by Eqs. (18) and (19) are equal to those obtained if the Ritz method is applied in its standard form to the linear pre-buckling and buckling problems [25, 29].

The second-order equations, i.e. those corresponding the initial post-buckling range, are readily available as:

$$\begin{cases} \mathbf{S}^{cc}\mathbf{c}^{(2)} + \mathbf{S}^{c\Phi}\mathbf{\Phi}^{(2)} = -\dfrac{1}{2}{\mathbf{w}^{(1)}}^{\mathrm{T}}\hat{\boldsymbol{\mathcal{N}}}_k\mathbf{w}^{(1)} \\ \mathbf{S}^{\Phi c}\mathbf{c}^{(2)} + \mathbf{S}^{\Phi\Phi}\mathbf{\Phi}^{(2)} = -\dfrac{1}{2}{\mathbf{w}^{(1)}}^{\mathrm{T}}\boldsymbol{\mathcal{N}}_{pq}\mathbf{w}^{(1)} \\ \mathbf{K}^{ww}\mathbf{w}^{(2)} + \left({\mathbf{c}^{(0)}}^{\mathrm{T}}\hat{\boldsymbol{\mathcal{N}}}_{mn} + {\mathbf{\Phi}^{(0)}}^{\mathrm{T}}\boldsymbol{\mathcal{N}}_{mn}\right)\mathbf{w}^{(2)} = \mathbf{0} \end{cases} \tag{21}$$

One can observe that the last equation is identically satisfied by taking $\mathbf{w}^{(2)} = \mathbf{0}$, meaning that the second-order solution regards the in-plane response only, i.e. it is associated with a variation of the internal membrane forces, but not the deflected surface. Thus, the corresponding number of degrees of freedom is (P+1)(Q+1), with K+1 additional dofs in case of prescribed displacement.

The solution of the initial post-buckling problem is indeed simplified to the solution of the first two equations reported in Eq. (21), which is a linear system in the unknowns $\mathbf{c}^{(2)}$ and $\mathbf{\Phi}^{(2)}$. Indeed, the quadratic terms in the amplitudes $\mathbf{w}^{(1)}$ can be calculated once the first-order solution is available, and represent the forcing term of the initial post-buckling problem.

2.3 Post-buckling response

The perturbation approach consists in the sequential solution of the three problems reported by Eqs. (18)-(21), and allows to determine the initial post-buckling behaviour by solving linear problems only.

One of the main advantage of the procedure relies on the possibility of quickly obtaining an estimate of the plate response in terms of the so-called first and second post-buckling coefficients a and b, which are the quantities associated with the asymptotic expansion of the load parameter as:

$$\begin{aligned} \lambda &= \lambda_{\mathrm{cr}} + \lambda_{\mathrm{cr}} a\xi + \lambda_{\mathrm{cr}} b\xi^2 + \cdots \\ &= \lambda_{\mathrm{cr}}\left(1 + b\xi^2\right) \end{aligned} \tag{22}$$

For the plate-type VS configurations anticipated in the current investigations, the first post-buckling coefficient a is assumed to be zero here and in all subsequent derivations. The second post-buckling coefficient b is given by [56]:

$$\begin{aligned} b &= -\frac{2F^{(1)}\left(w^{(1)}, w^{(2)}\right) + F^{(2)}\left(w^{(1)}, w^{(1)}\right)}{\lambda_{\mathrm{cr}}\hat{\Delta}} \\ &= -\frac{F^{(2)}\left(w^{(1)}, w^{(1)}\right)}{\lambda_{\mathrm{cr}}\hat{\Delta}} \end{aligned} \tag{23}$$

The expression of Eq. (23) is simplified due to the fact that $w^{(2)}$, for a flat plate, is identically null, and use is made of the short notation due to Hutchinson and Frauenthal [60], where:

$$A \cdot (B, C) = \int_{-l_x/2}^{+l_x/2} \int_{-l_y/2}^{+l_y/2} [A_{,xx} B_{,y} C_{,y} + A_{,yy} B_{,x} C_{,x} - A_{,xy} (B_{,x} C_{,y} + B_{,y} C_{,x})] \, \mathrm{d}x \, \mathrm{d}y \tag{24}$$

and:

$$\hat{\Delta} = \left. \frac{\partial F^{(0)}}{\partial \lambda} \right|_{\lambda=\lambda_{\mathrm{cr}}} \cdot (w^{(1)}, w^{(1)}) = F^{(0)} \cdot \left(w^{(1)}, w^{(1)} \right) \tag{25}$$

Another useful parameter for characterizing the post-buckling response is the slope of the force-displacement curve, i.e. the post-buckling stiffness. Within the present perturbation approach, the average membrane resultant along x reads:

$$\hat{N}_{xx} = \lambda \hat{N}_{xx}^{(0)} + \xi \hat{N}_{xx}^{(1)} + \xi^2 \hat{N}_{xx}^{(2)} \tag{26}$$

where the caret denotes the average load acting along the loaded edges of length. The expression of the generic term $\hat{N}_{xx}^{(i)}$ is available from Eqs. (11) and (15) and, in particular, it is:

$$\hat{N}_{xx}^{(i)} = -\frac{2}{b^2} \int_{-1}^{1} L_k \mathrm{d}\eta \; c_k^{(i)} \tag{27}$$

Or, in compact form, it can be written as:

$$\hat{N}_{xx} = \lambda \mathbf{N}^c \mathbf{c}^{(0)} + \xi \mathbf{N}^c \mathbf{c}^{(1)} + \xi^2 \mathbf{N}^c \mathbf{c}^{(2)} \tag{28}$$

where the expression of $\mathbf{N}^c$ is reported in the Appendix, while the vectors $\mathbf{c}^{(i)}$ are solutions of Eqs. (18), (20) and (21).

A closed-form solution can be derived for the nondimensional post-buckling stiffness, as the ratio between the stiffness just after the bifurcation and the linear stiffness in the pre-buckling range. In particular:

$$K_{\mathrm{pb}} = \frac{\hat{N}_{xx} - \hat{N}_{xx}^{\mathrm{cr}}}{\Delta - \Delta_{\mathrm{cr}}} \tag{29}$$

where the axial shortening is readily available as:

$$\Delta(\lambda) = \lambda \overline{u} \tag{30}$$

Using Eqs. (26) and (30), it is possible to re-write Eq. (29) as:

$$K_{\mathrm{pb}} = \frac{\lambda \hat{N}_{xx}^{(0)} + \xi \hat{N}_{xx}^{(1)} + \xi^2 \hat{N}_{xx}^{(2)} - \lambda_{\mathrm{cr}} \hat{N}_{xx}^{(0)}}{\lambda \overline{u} - \lambda_{\mathrm{cr}} \overline{u}} \tag{31}$$

Recalling now Eq. (22), and observing that $N_{xx}^{(1)}$, the perturbation parameter is expressed as:

$$\xi^2 = \left(\frac{\lambda}{\lambda_{\mathrm{cr}}} - 1 \right) \frac{1}{b} \tag{32}$$

and, after substitution of Eq. (32) into Eq. (31), it is obtained the expression of the post-buckling stiffness:

$$K_{\mathrm{pb}} = \frac{1}{(\lambda - \lambda_{\mathrm{cr}})\,\overline{u}} \left[(\lambda - \lambda_{\mathrm{cr}})\,\hat{N}_{xx}^{(0)} + (\lambda - \lambda_{\mathrm{cr}})\,\frac{1}{b\lambda_{\mathrm{cr}}}\hat{N}_{xx}^{(2)} \right] \tag{33}$$

Observing now that the linear pre-buckling stiffness is:

$$K_{\mathrm{pre}} = \frac{\lambda_{\mathrm{cr}}\hat{N}_{xx}^{(0)}}{\lambda_{\mathrm{cr}}\overline{u}} \tag{34}$$

It follows that:

$$K_{\mathrm{r}} = \frac{K_{\mathrm{pb}}}{K_{\mathrm{pre}}} = 1 + \frac{\hat{N}_{xx}^{(2)}}{b\hat{N}_{xx}^{\mathrm{cr}}} \tag{35}$$

where K_{r} is commonly denoted as relative post-buckling stiffness, which provides a measure of the post-buckling stiffness in relation the pre-buckling one.

It is important to highlight that the parameters characterizing the post-buckling response, such as the b-coefficient of Eq. (23) and the relative post-buckling stiffness of Eq. (35), are evaluated during the post-processing phase, once the solution of the second-order problem is available. Overall the procedure is very efficient and all the parameters can be derived with reduced computational effort. Furthermore, once the solution is available for a nominally perfect structure, the effect of initial imperfections can be easily recovered with no need to perform additional analyses. Assuming that the imperfection can be represented with the same shape of the first buckling mode, the relation due to Lanzo et al. [61] can be used:

$$\left(1 - \frac{\lambda}{\lambda_{\mathrm{cr}}}\right)\xi + b\left(\xi^3 + 2\xi\overline{\xi}^2 + 3\xi^2\overline{\xi}\right) = \frac{\lambda}{\lambda_{cr}}\overline{\xi} \tag{36}$$

where $\overline{\xi}$ is the nondimensional imperfection amplitude, defined as the ratio between the maximum imperfection value and the plate thickness.

3 Results

In this section, the results obtained using the perturbation approach are presented for a wide set of configurations, ranging from isotropic materials to composite ones with straight and curvilinear fibers.

The present approach will be referred to as reduced-order, in contrast to the classical Ritz multi-modal approach (see Refs. [25, 29, 33]), denoted hereinafter as the full-order one.

For clarity, the elastic properties of the materials considered in this section are summarized in Table 1.

To fully illustrate the potentialities of the formulation, different sets of loading and boundary conditions are discussed. A first part is devoted to the validation of the approach, as well its implementation, and the comparison against reference results from the literature is presented. In the second part, the potentialities of the approach are illustrated by exploring the design space for a set of variable-stiffness configurations. Design charts summarizing their post-buckling response, for which thousands of non-linear analyses are necessary,

are derived with reduced computational effort, and presented as a valuable tool for assisting the design phase. In all the analyses, the number of trial functions is specified as $A \times B$, where A stands for the number of functions along x, and B represents those along y.

3.1 Comparison against reference results

Isotropic and orthotropic plates under compression

The first example deals with isotropic and orthotropic composite panels, for which well-known closed-form solutions are available. In particular, the solutions derived in Refs. [62–65] are considered in terms of relative post-buckling stiffness K_{r}. The referenced works provide approximate solutions based on classical Koiter's approach [62] and Galerkin-type solution of von Kármán large deflection equations, where the compatibility equation is satisfied in exact manner [63–65].

Two materials are considered, an isotropic one with Poisson's ratio of 0.3 and Material A of Table 1. The plates are loaded in compression by means of a prescribed axial shortening, and they are simply-supported along the four-sides. Two different sets of in-plane conditions are considered for the longitudinal edges: in one case they are subjected to stress free conditions, and in the second case they are constrained to remain straight.

A summary of the results is provided in Table 2, where different plate aspect ratios are considered. One may observe that identical results are obtained up to the first four figures for all the cases investigated here, thus providing evidence of the ability of the present implementation to correctly capture the response of isotropic and orthotropic plates.

The existence of closed-form solutions is restricted to simply-supported boundary conditions. To verify the accuracy of the predictions for different sets of constraints, the results presented referring to the test cases presented by Lanzo et al. [61] and Rahman [39]. Different aspect ratios and flexural boundary conditions are considered. In all the cases, the load is introduced by means of a prescribed compressive force, whilst the longitudinal edges are subjected to in-plane stress-free conditions. The material is isotropic with Poisson's coefficient of 0.25. A preliminary convergence study is illustrated in Table 3, where the b-coefficients are reported for an increasing number of trial functions. The expansions are taken by considering the same number of trial functions for the stress function and the out-of-plane deflections. Furthermore, an equal number of P functions is considered along both directions. The number of integration points is set to P+5. It can be noted that, for all the cases reported, convergence is guaranteed up to the first four digits if 11 functions are used. This implies that the solution is achieved by solving linear problems of dimension 121. It is worth highlighting that good predictions are available even if the number of functions is restricted to 9, corresponding to the solution of linear problems of dimension 81. In this case, the maximum difference with respect to the convergence solution is below 0.3%. These results illustrate also that very few degrees

of freedom are generally required for obtaining converged results, much less than those required even by a relatively coarse finite element mesh. For instance, if a 25 $\times$ 25 thin-plate-element mesh is considered – similarly to the cases discussed in Ref. [61] – the number of degrees of freedom would be beyond 2000.

The comparison against the finite element perturbation approach due to Lanzo et al. [61] and Rahman [39] is presented in Table 4. Note that, for the latter, the results considered here are those obtained using the eight-node quadrilateral iso-parametric CQ40S shell element.

Based on the previous convergence study, calculations are conducted using 11 trial functions for approximating the unknown functions.

The results are presented in Table 4 in terms of linear buckling load and b-coefficient. Both in case of linear and non-linear calculations, they tend to lie in between those of Refs. [39, 61], demonstrating good accuracy irrespective on the aspect ratio and boundary conditions. Regarding bifurcation buckling loads, for which exact results are available, one can note that the results reported by Rahman [39] tend to be conservative, while the opposite is true for those of Ref. [61]. Thus the present solution closely corresponds to the exact solution. No exact solutions are available for the b-coefficients, but the agreement with reference ones is very good.

To further validate the present numerical model, the maximum out-of-plane deflections are reported for different load levels in Figure 3 for two of the plates reported in Table 4. Specifically, SCSC and SFCS boundary conditions are considered, and results are presented for different magnitudes of the initial imperfections w_0, taken equal to 0, 10% and 100% of the thickness of the plate. The results, consistently with those of Ref. [61], are presented in terms of total deviation from the nominally flat configuration. Thus, the sum of the imperfection and the post-buckling deflection is reported in the horizontal axis, while the nondimensional force $\overline{N}_{xx} = N^{\mathrm{cr}}_{xx} \left(\dfrac{\pi^2}{l_y^2} \dfrac{Eh^3}{12\left(1-\nu^2\right)} \right)^{-1}$ is reported at the vertical axis. Excellent agreement is observed with reference results, irrespective on the boundary conditions and amplitude of the initial imperfection. It is worth highlighting that one single analysis needs to be performed for a given plate configuration, and the effect of initial imperfection can be easily recovered ex-post by referring to Eq. (36).

Isotropic plates under in-plane bending

Buckling and post-buckling response are investigated in Table 5 for the case of in-plane bending, introduced by means of a prescribed force with linear distribution. The isotropic material is the same considered in the previous example, and the longitudinal edges are subjected to stress-free conditions.

In this case, the buckled surface tends to have a more complex pattern and, for this reason, several trial functions are generally necessary for guaranteeing convergence of the solution. This is particularly true for increasing values of the plate aspect ratio. To illustrate this aspect, analyses are conducted using 11×11 and 31×11 functions for approximating the unknown functions, where the number of functions is increased

along the longitudinal as suggested by the geometry of plates for which $r > 1$.

It is interesting to note that 11×11 functions are always sufficient to guarantee accurate buckling predictions, as no substantial advantages are achieved by enriching the basis up to 31 functions. On the contrary, an increase of the number of degrees of freedom is necessary when assessing the post-buckling response. This observation is particularly true for fully clamped panels, for which the errors in the evaluation of the b-coefficient can be as high as 22% if 11×11 functions are considered. As it turns out, a converged buckling analysis may not suffice to guarantee an accurate prediction of the b-coefficient, which, in general, demands for a higher accuracy in the description of the first-order modes. In other words, the buckling eigenvalue is stationary in the neighborhood of the eigenvector [66], thus refined descriptions of the modal shape are not necessary for capturing the bifurcation load. On the contrary, the same property does not hold with respect to the b-coefficient, and improved refinement is needed to guarantee accurate initial post-buckling description.

In this regard, the example highlights the importance of adopting relatively large basis of trial functions when plates are non-square and their post-buckling behaviour is of concern. This, in turn, highlights the need for an efficient implementation, capable of dealing with many degrees of freedom, while preserving the computational advantages inherently associated with the Koiter's approach.

Further proof of the good quality of the predictions is available in Figure 4, where the maximum out-of-plane displacements are plotted for different magnitudes of the initial imperfections against the calculations presented in [61]. Minor differences can be noted revealing a slight overstiffness in the reference results, presumably ascribable to the relatively coarse mesh adopted for calculations. The first-order mode is reported in the figure, illustrating a pattern with four half-waves in the compressively loaded region.

Cross-ply laminates under compression

Comparison against the single-term solution derived by Beerhorst et al. [67] for plates with rotationally restrained and free longitudinal edges is illustrated in Figure 5. Close agreement with FEM predictions was demonstrated in Ref. [67], so these results are believed to be an interesting benchmark for validating the present approach to the case of cross-ply laminates.

The plates are nominally flat and characterized by an aspect ratio equal to 3, with a longitudinal dimension of 600 mm, and are made of CFRP material B of Table 1. Two cross-ply stacking sequences are considered, $[0/90]_s$ and $[90/0]_s$, corresponding to a total thickness of 1 mm.

The panels are loaded with a prescribed axial shortening, and subjected to two sets of restraints, corresponding to SSSF and SCSF edges. The in-plane conditions are modeled by considering stress free edges, i.e. $N_{xy} = 0$ along the entire boundary and $N_{yy} = 0$ at the longitudinal edges. A slight difference should be pointed out with respect to the solution of Ref. [67], which is derived by considering one stress-free longi-

tudinal edge, free to translate along the in-plane direction, and another one constrained along the direction normal to the edge. However, due to the presence of one edge free to translate along the transverse direction, no significant membrane forces N_{yy} develop. The discrepancy between the two models is thus restricted to the local membrane force distribution in correspondence of the constrained longitudinal edge, which has a minor impact over the global response of the plate. Indeed very close agreement can be noticed in terms of maximum out-of-plane deflection at different load levels beyond the buckling load, as demonstrated by the plots of Figure 5. Clearly, the present approach does not offer the efficiency of the closed-form solution of Ref. [67]. However, the computational cost for one single run is still very low – of the order of $1/10$ s –, thus offering the advantage of allowing the analysis of a wider range of configurations with no restrictions on the lay-up, the distribution of the stiffnesses and the boundary conditions.

Variable-stiffness laminates under compression

Previous composite configurations were restricted to cross-ply lay-ups, for which the problem, in general, can be analytically tractable. More realistic configurations imply the presence of plies at orientations other than 0 and 90, which are those considered in the next example, starting from the results reported by Rahman [39]. Furthermore, the case of plates with variable-stiffness properties is considered, where the fiber orientation is allowed to vary between two values at the center and the edge of the panel according to Eq. (5).

The results are reported in Table 6, and refer to square simply-supported panels, made of Material A. Different sets of in-plane constraints are assumed, while the load is introduced in the form of a prescribed displacement.

The buckling loads are reported in nondimensional form, along with two nondimensional measures of the post-buckling stiffness, $K_{\mathrm{pb}}/K_{\mathrm{pre,iso}}$ and K_{r}, where K_{pb} is the post-buckling stiffness of the plate and $K_{\mathrm{pre,iso}}$ the linear stiffness of a quasi-isotropic configuration.

Following Ref. [39], and for comparison purposes, flexural anisotropy is artificially set to zero. Overall the results demonstrate close agreement, with post-buckling stiffnesses differing by less than 3% for all the configurations apart from the variable-stiffness one with boundary conditions B. In this case, two clustered modes are observed, the second one characterized by a lower post-buckling stiffness. For this lay-up, a higher discrepancy can be noted with respect to reference results, with percent differences of approximately 3% and 8% for the first and second mode, respectively. It is worth noting that results of Ref. [39] are presumably not completely converged and, indeed, a convergence study demonstrates that noticeable increase is achieved in the post-buckling stiffness by refining the mesh grid from 10 to 20 elements per side. It is thus believed that the discrepancy observed would be reduced if the analyses in the referenced work were run with a further refined mesh. Indeed, the aggressive steering of the $[90\pm < 0| - 75 >]_{4s}$ lay-up is responsible for drastic variations of the in-plane stiffnesses, rendering a refined in-plane approximation particularly important.

An interesting case is the one proposed by Madeo et al. [41] and Oliveri et al. [37], regarding a square

variable-stiffness plate with planar dimensions equal to 1000 mm and total thickness 1.5264 mm. The plate is made of material A with lay-up $[0\pm < 45|0 >]_{3s}$. Fully clamped conditions are considered, while the load is introduced in the form of a prescribed axial compressive force.

The nondimensional axial force is traced against the out-of-plane deflections in Figure 6. The predictions obtained with the present reduced-order approach are derived by with approximating the problem unknowns with 11 trial functions along both the directions x and y. The comparison is illustrated with the results derived by Madeo et al. [41] referring to a finite element-based Koiter's approach, and those presented by Oliveri et al. [37] by means of a displacement-based Ritz approach. Furthermore Abaqus results taken from Ref. [37] are presented as an additional comparison. Close agreement is observed with the reference results, especially with respect to those of Ref. [37], while the present results and the Ritz and Abaqus results of Ref. [37] show a stiffer behaviour than the results of Ref. [41].

It is interesting to discuss these results in terms of number of degrees of freedom according to the different solution strategies. Specifically, the results of Ref. [41] are obtained using a 100×100 mesh of 4-node elements with six degrees of freedom per node. It follows that the size of the problem is of the order of ten thousands, similarly to the converged finite element model of Ref. [37], consisting of 47526 dofs; the Ritz model of Ref. [37] makes use of 864 dofs. The present implementation allows to obtain converged results by solving linear problems of size 121, which reveals the efficiency of the formulation with consequent beneficial effects on the computational time.

It is worth highlighting that the advantages of the proposed approach are very clear when analysing specific test cases and simple structures, such as those outlined in this section. The advantages become even more important when thousands of analyses are performed, as it commonly happens in preliminary studies and design optimizations. Clearly, the larger number of degrees of freedom and corresponding higher computational time of a finite element model is substantially compensated by a larger field of employ, allowing the study of structures with more general and complex geometries. It follows that the proposed Ritz-based approach has not to be interpreted as an alternative to finite element strategies. Rather it as a highly efficient way for handling problems characterized by simple geometries for which the understanding of the underlying mechanical response is of concern.

For completeness, it is noted that shear deformability is not accounted for in the context of the proposed approach, while it is considered in the approaches of Refs. [37, 41]. Furthermore, the solution procedure implemented exploits the uncoupling of membrane and bending behaviour, so that the size of the problem is kept at a minimum.

To further investigate the case of variable-stiffness plates, two examples presented by Wu et al. [33] are illustrated in terms of force-displacement and force-maximum deflection plots in Figure 7.

Square panels made of Material C are considered, with lay-ups of $[0\pm < 0|20 >]_{4s}$ and $[90\pm < 0|75 >]_{4s}$. The former is characterized by a fiber variation along the longitudinal direction, the latter along the trans-

verse one, which leads to superior buckling performance due to pre-buckling load redistribution towards the edges. The boundaries are simply-supported, with the longitudinal sides free to expand but forced to remain straight. The load is introduced by means of a prescribed displacement.

The force-displacement plot of Figure 7(a) is reported in a nondimensional form, using the quasi-isotropic configuration as a reference. One can observe the excellent agreement in terms of drop of stiffness in correspondence of the bifurcation point for both the configurations. Given the lowest buckling load of the $[0\pm<0|20>]_{4s}$ laminate, a deeper post-buckling region is shown in the plot. It is interesting to highlight the increasing loss of accuracy of the present approach, which relies upon a linearization around the bifurcation load, far from the initial post-buckling range. This aspect is further clarified in Figure 7(b), where the first-order mode is reported along with the post-buckling pattern calculated at $\hat{N}_{xx}/N_{xx,\text{iso}} = 3.5$ by implementing the full-order Ritz method of Ref. [33]. It can be observed that the deformed configuration and the first-order mode of the $[90\pm<0|75>]_{4s}$ laminate are very similar each other, thus justifying the close agreement between the present solution and reference one. On the contrary, the $[0\pm<0|20>]_{4s}$ laminate experiences a progressive change of pattern, whose final configuration is presented in Figure 7(b), as the structure enters the moderate/deep post-buckling field, whose modal interactions cannot be predicted by the present formulation.

Comparison between reduced-order and full model

The comparison between the predictions obtained using the reduced-order and a full model is further investigated by considering additional variable-stiffness configurations.

Specifically, two exemplary test cases are presented to show that the accuracy of the reduced-order predictions depends on two main aspects, namely the degree of non-linearity due to the post-buckling deflections, as well as modal interactions in the post-critical regime.

To this aim, two square panels made of Material C are considered. The lay-ups are $[90\pm<0|15>]_{4s}$ and $[90\pm<0|75>]_{4s}$. Simply-supported constraints, with straight transverse edges are considered, while the load is imposed by prescribing the axial shortening. The plots summarizing the post-buckling response in terms of force-displacement curve and maximum out-of-plane deflections are presented in Figure 8 using the reduced-order model and the full one. As expected, close results are achieved in the surrounding of the bifurcation load, while the accuracy of the reduced-order model tends to diminish far away from it. For a given load level, the accuracy tends to be smaller for those configurations undergoing larger out-of-plane displacements. This behaviour is indeed observed from Figure 8. This behaviour is reflected into the membrane resultant distribution at the loaded edges, which is reported for two load levels in Figure 9, along with first-order modes and post-buckled patterns.

It is interesting to extend the investigation to variable-stiffness plates with lay-ups $[90\pm<90|15>]_{4s}$ and $[90\pm<90|75>]_{4s}$. As seen from the post-buckling curves of Figure 10, the situation is now reversed,

as lower accuracy is associated with the configuration undergoing the smallest out-of-plane displacements. This behaviour is understood by assessing the membrane load distribution and the post-buckling patterns reported in Figure 11. As observed from Figure 11(a), the quality of the initial post-buckling predictions for $\Delta/\Delta_{\rm cr} = 1.1$ is satisfactory, and the reduced-order model provides results in close-agreement with those of the full model. When the load is increased up to $\Delta/\Delta_{\rm cr} = 4.0$, a progressive change of the post-buckled shape is observed for the $[90\pm < 90|75 >]_{4s}$ laminate, leading to a pattern which significantly deviated from the first-order mode. This, in turn, determines a loss of accuracy in the description of the membrane state of stress. It follows that, despite the lower degree of non-linearity in terms of out-of-plane deflections, the prediction for the $[90\pm < 90|75 >]_{4s}$ configuration tends to be less accurate.
As a rule of thumb, one can consider $\Delta/\Delta_{\rm cr} = 1.5$ as the upper bound for guaranteeing satisfactory accuracy of the results in most of the cases.

3.2 Design charts

The advantage of the present formulation relies upon the combined reduced computational cost along with a wide field of employ in terms of lay-up, boundary and loading conditions. In a nutshell, the formulation tries to combine the ease of computation of closed-form solutions with the range of applicability of more costly non-linear Ritz- or FEM-like calculations.
This feature can be exploited for performing several analysis very quickly, which is particularly useful for obtaining design charts to explore the buckling and post-buckling behaviour of variable-stiffness configurations. For instance, the contour plots of Figures 12 to 15 span the entire design space of laminates with lay-ups $[\Phi\pm < T_0|T_1 >]_{4s}$, different aspect ratios and subjected to various loading and boundary conditions. In-plane stress free boundary conditions are assumed unless otherwise specified.
The charts are realized by allowing T_0 and T_1 to vary from 0 to 90 degrees with steps of 1 degree, thus corresponding to more than 8000 analyses.
Following Wu et al. [33], the results are presented in nondimensional form by taking a quasi-isotropic configuration as reference. Specifically, a design load equal to 1.50 times the critical load of the quasi-isotropic configuration is assumed. The results are reported in terms of nondimensional buckling force $\hat{N}^{\rm cr}_{xx}/N_{xx,{\rm iso}}$, post-buckling stiffness $K_{\rm pb}/K_{\rm pb,iso}$ and maximum out-of-plane deflections $w_{\rm max}/w_{\rm max,iso}$.
In addition, the relative post-buckling stiffness $K_{\rm r}$, defined as the ratio between the post- and pre-buckling stiffness, is presented, as it provides a useful information regarding the effect of buckling in terms of drop of stiffness which, in turn, has an impact over the internal load path of the structure.

Simply-supported square plates loaded in compression

The first case, whose results are depicted in Figure 12, regards a square simply-supported panel loaded with a prescribed displacement. The lay-up is $[90\pm < T_0|T_1 >]_{4s}$, so the fibers change their orientation along the transverse direction y. A number of 13×13 functions is considered, based on a preliminary convergence study. To further remark the efficiency of the method, it is observed that one single run requires, on average, 0.20 s on a standard laptop with Intel Core i7 and 32 GB of RAM. It is interesting to note that the CPU time is approximately 5 to 10 times faster with respect to an already efficient Ritz full-order implementation. This amount of speed-up is particularly beneficial in case of repeated analyses, such as for the generation of the design charts discussed here. In this case, the advantage is multiplied by a factor equal to the number of analyses to be run. i.e. 8000.

As observed from Figure 12(a), the highest buckling loads are achieved for $T_0 = 0$ and $T_1 = 77$, which correspond to an in-plane stiffness distribution, where loads are mostly supported at the plate edges. Looking at the post-buckling stiffness in Figure 12(b), one can observe that the highest values are achieved in the top right region, i.e. with fibers aligned along the loading direction (T_0 and T_1 close to 90). These configurations are clearly associated with poor buckling performance. It is interesting to observe that, starting from a given angle T_0, the post-buckling stiffness can raised by increasing T_1 towards higher angles of orientation. This means that rotating the outer fibers along the loading direction promotes post-buckling load-carrying capability. This is not necessarily the case if one is interested in the relative post-buckling stiffness K_{r}, whose response is depicted in Figure 12(c). Highest values are achieved in a region associated with relatively high buckling loads, although a one-to-one correspondence is be found. A frontier of discontinuity can be seen in the plot, which is due to a change of shape of the first-order mode. Looking at the maximum out-of-plane deflections, one can observe an approximately inverse trend with respect to the buckling chart. Indeed, higher buckling loads have the effect of reducing the post-buckling region which the panel is exposed to for sustaining the prescribed design load. Whenever the buckling load is higher than the prescribed load, the plate remains unbuckled, as seen for the configurations in the blue region of Figure 12(d). It is worth noting that configurations lying on the same buckling plot isolines do not necessarily share the same response in terms of maximum out-of-plane deflections, thus requirements over the maximum deflections can discriminate the choice between buckling-equivalent configurations.

The same configurations, but considering now aspect ratio equal to 3, are studied in Figure 13. This geometry is closer to typical aerospace panels, and the presence of longer edges has the effect of reducing the effects due to the boundaries. This example is a challenging one, as adequate spatial refinement is needed. Due to the increased aspect ratio and the corresponding larger number of buckling half-waves, 25×13 trial functions were found to be necessary to guarantee convergence.

While buckling and post-buckling stiffness charts (Figures 13(a) and 13(b)) are almost unchanged, it is interesting to note the altered pattern of the relative post-buckling stiffness (Figure 13(c)). In this case,

multiple sudden variations exist due to a different distribution of mode shapes in the design space T_0-T_1. Looking at the maximum out-of-plane displacements in Figure 13(d), it is possible to note a similar pattern with respect to the one obtained for square plates (see Figure 12(d)). However, the magnitude of deflections is different, meaning that plate geometric effects are relevant. For this reason, any design choice involving the post-buckling deflections should be carefully taken by referring to the actual geometric configuration, and reference solutions available for square plates can provide qualitative but not quantiative information.

Plates with one free edge loaded in compression

The response of plates with SSSF boundary conditions and aspect ratio equal to 10 is presented in Figure 14. Fiber steering is now permitted along the longitudinal direction x, with lay-ups in the form of $[0\pm < T_0|T_1 >]_{4s}$. These configurations can be representative of the web of a blade stringer or the flange of a T stringer. In this context, one may be interested in assessing not only the buckling load, but also the behaviour in the post-buckling regime. The presence of a free-edge determines a buckling chart which is quite different form the previous ones, the optimal region being now in the central part of the design space (see Figure 14(a)), i.e. plies at ± 45. On the contrary, high post-buckling stiffness is still achieved when fibers are mostly directed along the loading direction, in this case corresponding to T_0 and T_1 equal to 0. The reason here is to be attributed to the much higher linear stiffness of 0-degree plies, which leads to an equally higher post-buckling stiffness. Indeed, the relative post-buckling stiffness varies in a restricted range of values (see Figure 14(c)), so the prevailing effect is the one of the pre-buckling stiffness.
Out-plane-deflections are depicted in Figure 14(d). It is interesting to observe that requirements over the maximum out-plane-displacements can be satisfied by preventing the values of T_0 and T_1 to exceed a given threshold. In other words, the post-buckling deflections tend to increase as fibers are rotated more and more transversally with respect to the loading direction. Also, it can be observed that the response of straight fiber designs, i.e. points lying on the diagonal of the plot, can be generally improved thanks to fiber steering.

Fully clamped plate under in-plane bending

Another example regards loading condition of pure in-plane bending, applied at the short edges of plates with aspect ratio equal to 3 and fully clamped at the four sides. Given the relatively complex shapes of the first order modes, a number of functions equal to 25×13 is adopted.
The results are reported in terms of buckling load, Figure 15(a), and maximum out-of-plane deflection, Figure 15(b). The presence of an unbuckled region can be observed in Figure 15(b), for those configurations associated with a buckling load higher than the design load. In general, it can be noted that contemporary increase of buckling loads and reduction of post-buckling deflections are possible thanks to fiber steering. The plots of Figure 15 can help to quantify these aspects.

4 Conclusions

The paper presented a formulation based on Koiter's perturbation theory for analyzing the post-buckling behaviour of variable-stiffness plates. Isotropic and composite plates can be retrieved as a special case. The approach relies upon a mixed variational principle, where the unknowns are described by means of global Ritz-like functions. The kinematic approach relies on von Kármán theory, so the formulation can be successfully employed in those cases where post-bucking stress redistribution is noticeable, such as the plate configurations and the corresponding specific boundary conditions as investigated in this paper. Beam-like plates, for which the redistribution effects are milder, would require the adoption of more advanced kinematic formulations. The nonlinear post-buckling problem is solved after performing a linearization around the bifurcation point, which transforms the non-linear governing equations into a series of linear equations. The implementation of the approach is restricted to the single-mode case and leads to a highly efficient numerical tool, which can be successfully employed for estimating the initial post-buckling response of variable-stiffness plates. Main advantage is to be found in the computational effectiveness of the method, which allows to deal with a small number of degrees of freedom, generally of the order of the hundreds, much less than those typically required by a finite element approximation. When compared to a similar full-order, Ritz-based approach – for which a comparison of the computational times can be easily performed –, the time saving is, approximately, of one order of magnitude. The improved efficiency of the approach is particularly suitable for analyzing simple geometries, such as the plates considered in this paper, that can help to derive benchmark results and gather insight into the mechanical behaviour of variable-stiffness configurations. In this regard, the cases presented in the paper have practical significance for aircraft structures, and are representative of the skin of a stiffened panel undergoing local buckling, or the flanges of blade stiffeners. More complex configurations are beyond the scopes of the Ritz approach and, to this aim, finite element procedures can be the most viable strategy.

The accuracy of the predictions is demonstrated by means of an extensive set of comparisons against results from the literature. As observed, the quality of the predictions tends to decrease as the structure enters the moderate to deep post-buckling regime. However, if the range of interest is not too far away from the bifurcation and modal interactions are not relevant, the proposed strategy is capable of furnishing accurate results.

The efficiency of the formulation is particularly useful for gathering understanding into the mechanical behaviour of variable-stiffness plates, where the number of design variables is even higher than in classical composite configurations. This aspect is of paramount importance to guide the design, especially when non-linear responses are of concern. Design charts can be easily derived, and parametric studies or preliminary optimizations can be conducted with reduced effort. The extension to include shear deformability effects and the possibility of accounting multi-modal interactions are subject of future investigation.

5 Acknowledgements

Part of the work presented in this paper has been done during the research stay of the second author (Enrico Spigarolo) at Leibniz University Hannover, the institute of Prof. Rolfes, Institute of Structural Analysis.

References

[1] A. Deturk, R. Diaz, G. Digiovanni, and B.I. Hyman. Exploratory tests on fiber-reinforced plates with circular holes under tension. *AIAA Journal*, 7(9):1820–1821, 1969.

[2] A.W. Leissa and A.F. Martin. Vibration and buckling of rectangular composite plates with variable fiber spacing. *Composite Structures*, 14(4):339–357, 1990.

[3] M.W. Hyer and R.F. Charette. Use of curvilinear fiber format in composite structure design. In 30^{th} *AIAA Structures, Structural Dynamics, and Materials Conference*, 89-1404-CP, Mobile, AL, 3–5 April 1989.

[4] M.W. Hyer and R.F. Charette. Use of curvilinear fiber format in composite structure design. *AIAA Journal*, 29(6):1011–1015, 1991.

[5] Z. Gürdal and R. Olmedo. Composite laminates with spatially varying fiber orientations: variable stiffness panel concept. In 33^{rd} *AIAA/ASME/ASCE/AHS/ASC Structures, Structural Dynamics and Material Conference*, Dallas, TX, April 13–15 1992.

[6] R. Olmedo and Z. Gürdal. Buckling response of laminates with spatially varying fiber orientations. In 34^{th} *AIAA/ASME/ASCE/AHS/ASC Structures, Structural Dynamics and Material Conference*, La Jolla, CA, April 19–22 1993.

[7] B.F. Tatting and Z. Gürdal. Analysis and design of tow-steered variable stiffness composite laminates. In *AHS Meeting*, Williamsburg, VA, 30 October–1 November 2001.

[8] Z. Gürdal, B.F. Tatting, and C.K. Wu. Variable stiffness composite panels: effects of stiffness variation on the in-plane and buckling response. *Composites Part A: Applied Science and Manufacturing*, 39(5):911–922, 2008.

[9] R. Vescovini and L. Dozio. Thermal buckling behaviour of thin and thick variable-stiffness panels. *Journal of Composites Science*, 2(4):1–23, 2018.

[10] G. Manickam, A. Bharath, A.N. Das, A. Chandra, and P. Barua. Thermal buckling behaviour of variable stiffness laminated composite plates. *Materials Today Communications*, 16:142–151, 2018.

[11] M.M. Abdalla, S. Setoodeh, and Z. Gürdal. Design of variable stiffness composite panels for maximum fundamental frequency using lamination parameters. *Composite Structures*, 81(2):283–291, 2007.

[12] H. Akhavan and P. Ribeiro. Natural modes of vibration of variable stiffness composite laminates with curvilinear fibers. *Composite Structures*, 93(11):3040–3047, 2011.

[13] S. Yazdani and P. Ribeiro. A layerwise p-version finite element formulation for free vibration analysis of thick composite laminates with curvilinear fibres. *Composite Structures*, 120:531–542, 2015.

[14] F. Tornabene, N. Fantuzzi, M. Bacciocchi, and E. Viola. Higher-order theories for the free vibrations of doubly-curved laminated panels with curvilinear reinforcing fibers by means of a local version of the GDQ method. *Composites Part B: Engineering*, 81:196–230, 2015.

[15] C. Lopes, P.P. Camanho, and Z. Gürdal. Progressive failure analysis of tow-placed, variable-stiffness composite panels. *International Journal of Solids and Structures*, 44(25-26):8493–8516, 2007.

[16] A. Khani, S.T. IJsselmuiden, M. Abdalla, and Z. Gürdal. Design of variable stiffness panels for maximum strength using lamination parameters. *Composites Part B: Engineering*, 42(3):546–552, 2011.

[17] F. Tornabene, N. Fantuzzi, and M. Bacciocchi. Higher-order structural theories for the static analysis of doubly-curved laminated composite panels reinforced by curvilinear fibers. *Thin-Walled Structures*, 102(102):222–245, 2016.

[18] L. Demasi, G. Biagini, F. Vannucci, E. Santarpia, and R. Cavallaro. Equivalent Single layer, Zig-Zag, and Layer Wise theories for variable angle tow composites based on the Generalized Unified Formulation. *Composite Structures*, 177:54–79, 2017.

[19] C.S. Sousa, P.P. Camanho, and A. Suleman. Analysis of multistable variable stiffness composite plates. *Composite Structures*, 98:34–46, 2013.

[20] A. Haldar, J. Reinoso, E. Jansen, and R. Rolfes. Thermally induced multistable configurations of variable stiffness composite plates: Semi-analytical and finite element investigation. *Composite Structures*, 183:161–175, 2018.

[21] P.M. Anilkumar, A. Aldar, E. Jansen, B.N. Rao, and R. Rolfes. Design optimization of multistable variable-stiffness laminate. *Mechanics of Advanced Materials and Structures*, pages 1–8, 2019.

[22] S. Setoodeh, M.M. Abdalla, S.T. IJsselmuiden, and Z. Gürdal. Design of variable-stiffness composite panels for maximum buckling load. *Composite Structures*, 87(1):109–117, 2009.

[23] S. IJsselmuiden, M.M. Abdalla, and Z. Gürdal. Optimization of variable-stiffness panels for maximum buckling load using lamination parameters. *AIAA Journal*, 48(1):134–143, 2010.

[24] M. Rouhi, H. Ghayoor, S.V. Hoa, and M. Hojjati. Computational efficiency and accuracy of multi-step design optimization method for variable stiffness composite structures. *Thin-Walled Structures*, 113:136–143, 2017.

[25] G. Raju, Z. Wu, B.C. Kim, and P.M. Weaver. Prebuckling and buckling analysis of variable angle tow plates with general boundary conditions. *Composite Structures*, 94(9):2961–2970, 2012.

[26] G. Raju, Z. Wu, and P.M. Weaver. Postbuckling analysis of variable angle tow plates using differential quadrature method. *Composite Structures*, 106:74–84, 2013.

[27] P. Hao, X. Yuan, H. Liu, B. Wang, C. Liu, D. Yang, and S. Zhan. Isogeometric buckling analysis of composite variable-stiffness panels. *Composite Structures*, 165:192–208, 2017.

[28] P. Hao, X. Yuan, C. Liu, B. Wang, H. Liu, G. Li, and F. Niu. An integrated framework of exact modeling, isogeometric analysis and optimization for variable-stiffness composite panels. *Computer Methods in Applied Mechanics and Engineering*, 339:205–238, 2018.

[29] Z. Wu, P.M. Weaver, G. Raju, and B.C. Kim. Buckling analysis and optimisation of variable angle tow composite plates. *Thin-Walled Structures*, 60:163–172, 2012.

[30] Z. Wu, G. Raju, and P.M. Weaver. Framework for the buckling optimization of variable-angle tow composite plates. *AIAA Journal*, 53(12):3788–3804, 2015.

[31] R. Vescovini and L. Dozio. A variable-kinematic model for variable stiffness plates: Vibration and buckling analysis. *Composite Structures*, 142:15–26, 2016.

[32] F. Li and G.J. Nie. Thermo-mechanical buckling analysis of symmetric VAT composite laminates with temperature-dependent material properties. *Thin-Walled Structures*, 140:263–271, 2019.

[33] Z. Wu, G. Raju, and P.M. Weaver. Postbuckling analysis of variable angle tow composite plates. *International Journal of Solids and Structures*, 50(10):1770–1780, 2013.

[34] Z. Wu, P.M. Weaver, and G. Raju. Postbuckling optimisation of variable angle tow composite plates. *Composite Structures*, 103:34–42, 1032013.

[35] Z. Wu, G. Raju, and P.M. Weaver. Optimization of postbuckling behaviour of variable thickness composite panels with variable angle tows: towards Buckle-Free design concept. *International Journal of Solids and Structures*, 132:66–79, 2018.

[36] V. Oliveri and A. Milazzo. A Rayleigh-Ritz approach for postbuckling analysis of variable angle tow composite stiffened panels. *Computers & Structures*, 196:263–276, 2018.

[37] V. Oliveri, A. Milazzo, and P.M. Weaver. Thermo-mechanical post-buckling analysis of variable angle tow composite plate assemblies. *Composite Structures*, 183:620–635, 2018.

[38] W.T. Koiter. On the stability of elastic equilibrium. Ph.D. Thesis, Tu-Delft, 1945. [in Dutch].

[39] T. Rahman. A perturbation approach for geometrically nonlinear structural analysis using a general purpose finite element codes. Ph.D. Thesis, TU-Delft, 2009.

[40] T. Rahman, S.T. Ijsselmuiden, M.M. Abdalla, and E. Jansen. Postbuckling analysis of variable stiffness composite plates using a finite element-based perturbation method. *International Journal of Structural Stability and Dynamics*, 11(4):735–753, 2011.

[41] A. Madeo, R.M.J. Groh, P.M. Weaver, G. Zagari, and R. Zinno. Post-buckling analysis of variable-angle tow composite plates using Koiter's approach and the finite element method. *Thin-Walled Structures*, 110:1–13, 2017.

[42] K. Liang, Q. Sun, and Y. Zhang. Nonlinear buckling analysis of variable stiffness composite plates based on the reduced order model. *Composite Structures*, 206:681–692, 2018.

[43] G. Garcea, F.S. Liguori, L. Leonetti, D. Magisano, and A. Madeo. Accurate and efficient a posteriori account of geometrical imperfections in Koiter finite element analysis. *International Journal for Numerical Methods in Engineering*, 112(9):1154–1174, 2017.

[44] F.S. Liguori, G. Zucco, A. Madeo, D. Magisano, L. Leonetti, G. Garcea, and P.M. Weaver. Postbuckling optimisation of a variable angle tow composite wingbox using a multi-modal Koiter approach. *Thin-Walled Structures*, 138:183–198, 2019.

[45] S. White, G. Raju, and P.M. Weaver. Initial post-buckling of variable-stiffness curved panels. *Journal of the Mechanics and Physics of Solids*, 71:132–155, 2014.

[46] G. Raju, Z. Wu, S. White, and P.M. Weaver. Optimal postbuckling design of variable angle tow composite plates. *AIAA Journal*, 56(5):2045–2061, 2018.

[47] S.C. White and P.M. Weaver. Towards imperfection insensitive buckling response of shell structures-shells with plate-like post-buckled responses. *The Aeronautical Journal*, 120(1224):233–253, 2016.

[48] C. Bisagni and R. Vescovini. Analytical formulation for local buckling and post-buckling analysis of stiffened laminated panels. *Thin-Walled Structures*, 47(3):318–334, 2009.

[49] C. Bisagni and R. Vescovini. Fast tool for buckling analysis and optimization of stiffened panels. *Journal of Aircraft*, 46(6):2041–2053, 2009.

[50] G. Garcea, A. Madeo, and R. Casciaro. Nonlinear fem analysis for beams and plate assemblages based on the implicit corotational method. *Journal of Mechanics of Materials and Structures*, 7(6):539–574, 2012.

[51] G. Garcea, A. Madeo, and R. Casciaro. The implicit corotational method and its use in the derivation of nonlinear structural models for beams and plates. *Journal of Mechanics of Materials and Structures*, 7(6):509–538, 2012.

[52] M.W. Hyer. *Stress Analysis of Fiber-Reinforced Composite Materials*. McGraw-Hill, New York, 1998.

[53] J.N. Reddy. *Mechanics of Laminated Composite Plates and Shells: Theory and Analysis*. CRC Press, Boca Raton, 2004.

[54] V. Giavotto. Sulla meccanica di pannelli di strutture aerospaziali. *Memorie dell' Istituto Lombardo - Accademia di Scienze e Lettere*, XXV(4), 1966. [Italian].

[55] V. Giavotto. Sulla meccanica dei pannelli anisotropi ed eterogenei. *Memorie dell' Istituto Lombardo - Accademia di Scienze e Lettere*, XXV(5), 1969. [Italian].

[56] J. Arbocz and J.M.A.M. Hol. ANILISA - computational module for Koiter's imperfection sensitivity theory. Report LR-245, TU Delft, 1989.

[57] J. Arbocz, J.M.A.M. Hol, and J. de Vries. The effect of initial imperfections on shell stability. In *Modern Problems of Structural Stability*, pages 117–228. Springer, 2002.

[58] J. Singer, J. Arbocz, and T. Weller. *Buckling Experiments: Experimental Methods in Buckling of Thin-Walled Structures: Basic Concepts, Columns, Beams and Plates, Volume 1.* Wiley, New York, 1998.

[59] R.M. Jones. *Buckling of Bars, Plates, and Shells*. Bull Ridge Corporation, Blacksburg, VA, 2006.

[60] J.W. Hutchinson and J.C. Frauenthal. Elastic postbuckling behavior of stiffened and barreled cylindrical shells. *Journal of Applied Mechanics*, 36(4):784–790, 1969.

[61] A.D. Lanzo, G. Garcea, and R. Casciaro. Asymptotic post-buckling analysis of rectangular plates by hc finite elements. *International Journal for Numerical Methods in Engineering*, 38(14):2325–2345, 1995.

[62] B. Budiansky. Theory of buckling and post-buckling behavior of elastic structures. *Advances in Applied Mechanics*, 14:1–65, 1974.

[63] G.Z. Harris. Buckling and post-buckling of orthotropic laminated plates. In 16^{th} *AIAA Structures, Structural Dynamics, and Materials Conference*, AIAA-1975-813, Denver, CO, May 27–29 1975.

[64] A. van der Neut. The stiffness in compression of imperfect elastically restrained plate strips at various in-plane boundary conditions. Report LR-245, TU Delft, 1977.

[65] R. Vescovini. Analytical formulation for buckling and post-buckling analysis and optimization of composite stiffened panels. Ph.D. Thesis, Politecnico di Milano, 2011.

[66] Z. Bažant and L. Cedolin. *Stability of Structures: Elastic, Inelastic, Fracture and Damage Theories*. World Scientific, Singapore, 1991.

[67] M. Beerhorst, M. Seibel, and C. Mittelstedt. Efficient approximate solutions for postbuckling of axially compressed orthotropic plates with rotationally restrained and free longitudinal edges. *Archive of Applied Mechanics*, 88(3):461–476, 2018.

Table 1: Elastic properties of CFRP composite materials.

Material	E_{11} (MPa)	E_{22} (MPa)	G_{12} (MPa)	ν_{12} (MPa)
A	181000	10273	7170.5	0.28
B	128000	11300	6000	0.3
C	163000	6800	3400	0.28

Table 2: Relative post-buckling stiffness K_{r} for SSSS plates under different in-plane constraints: comparison against closed-form solutions (A: stress-free transverse edges; B: transverse edges forced to remain straight).

	Isotropic				$[0/90]_s$			
In-plane BCs	A		B		A		B	
a/b	Ref. [64]	Present	Ref. [62]	Present	Ref. [65]	Present	Ref. [63]	Present
1.0	0.4083	0.4083	0.5000	0.5000	0.3654	0.3654	0.5000	0.5000
1.25	0.4509	0.4509	0.6324	0.6324	0.3824	0.3824	0.6324	0.6324
1.5	0.3683	0.3683	0.3969	0.3969	0.4001	0.4001	0.7519	0.7519
1.75	0.3872	0.3872	0.4423	0.4423	0.4176	0.4176	0.8384	0.8384
2.0	0.4083	0.4083	0.5000	0.5000	0.4343	0.4343	0.8947	0.8947

Table 3: Convergence analysis (P=Q=M=N=K): b-coefficients for isotropic plate ($\nu = 0.25$) subjected to prescribed compressive force.

N. trial functions		3×3	5×5	7×7	9×9	11×11	21×21
BC	$r = a/b$						
SSSS	1	0.1798	0.1827	0.1827	0.1827	0.1827	0.1827
	2	0.1454	0.2060	0.2121	0.2120	0.2120	0.2120
	3	0.0629	0.1724	0.2151	0.2221	0.2226	0.2226
SCSC	1	0.1467	0.1825	0.1953	0.1957	0.1957	0.1957
	2	0.0699	0.1983	0.2569	0.2650	0.2654	0.2654
SFSC	2	0.0088	0.0089	0.0089	0.0089	0.0089	0.0089
CSCS	2	0.1692	0.2391	0.2579	0.2603	0.2604	0.2604

Table 4: Nondimensional buckling loads and b-coefficients for isotropic plate ($\nu = 0.25$) subjected to prescribed compressive force.

		$\overline{N}_{xx} = N_{xx}^{\mathrm{cr}} \left(\frac{\pi^2}{l_y^2} \frac{Eh^3}{12\,(1-\nu^2)} \right)^{-1}$			b-coeff.		
BC	$r = a/b$	Ref. [61]	Ref. [39]	Present	Ref. [61]	Ref. [39]	Present
SSSS	1	4.0026	3.9599	4.0000	0.1824	0.1836	0.1827
	2	4.0032	/	4.0000	0.2118	/	0.2120
	3	4.0067	/	4.0000	0.2217	/	0.2226
SCSC	1	7.7135	7.6528	7.6913	0.1958	0.1962	0.1957
	2	7.0114	/	6.9716	0.2654	/	0.2654
SFSC	2	1.3881	1.3788	1.3862	0.0088	0.0090	0.0089
CSCS	2	4.8550	4.8239	4.8471	0.2608	0.2608	0.2604

Table 5: Nondimensional buckling loads and b-coefficients for isotropic plate subjected to in-plane bending (^{1},^{2}: using 11 and 31 functions along the longitudinal direction, respectively.)

		$\overline{N}_{xx} = N_{xx}^{\mathrm{cr}} \left(\frac{\pi^2}{l_y^2} \frac{Eh^3}{12\left(1-\nu^2\right)} \right)^{-1}$				b-coeff.			
BC	$r = a/b$	Ref. [61]	Ref. [39]	Present^1	Present^2	Ref. [61]	Ref. [39]	Present^1	Present^2
SSSS	1	25.5766	25.2295	25.5283	25.5283	0.2193	0.2212	0.2188	0.2188
	2	23.9452	23.6668	23.8818	23.8818	0.2196	0.2217	0.2239	0.2240
	3	24.2542	/	24.1119	24.1118	0.2115	/	0.2102	0.2119
CCCC	1	48.1574	/	47.7539	47.7539	0.2924	/	0.2926	0.2926
	2	42.2118	/	41.6466	41.6456	0.2858	/	0.2643	0.2775
	3	41.7225	/	40.6135	40.4789	0.2765	/	0.2229	0.2727

Table 6: Nondimensional buckling loads and post-buckling stiffnesses for square SSSS composite plates with straight and curvilinear fibers (B: transverse edges forced to remain straight; C: transverse edges prevented from lateral displacement). Results from Ref. [39] are reported in parenthesis.

		$\overline{N}_{xx} = \hat{N}^{\mathrm{cr}}_{xx}\left(\frac{E_{11}h^3}{l_x^2}\right)^{-1}$			
In-plane BCs	Lay-up	Mode 1	Mode 2	$K_{\mathrm{pb}}/K_{\mathrm{pre,iso}}$	K_{r}
C	quasi-isotropic	1.0709 (1.0681)	2.0191 (2.0106)	0.5207 (0.52113)	0.5207 (0.52113)
	$[\pm 32]_s$	1.1993 (1.1965)	2.6772 (2.6669)	0.2879 (0.29288)	0.2160 (0.21958)
	$[0\pm < 0\|50 >]_s$	1.4366 (1.4159)	2.7578 (2.6835)	0.3509 (0.35171)	0.2618 (0.26846)
B					
	quasi-isotropic	1.3878 (1.3842)	2.1685 (2.1594)	0.5000 (0.49363)	0.5000 (0.49363)
	$[\pm 45]_s$	1.7461 (1.7424)	2.3252 (2.2361)	0.1798 (0.17492)	0.5000 (0.48650)
	$[90\pm < 0\| - 75 >_s]$	3.1345 (2.9282)	3.1503 (2.9499)	0.4126 (0.38264)	0.7683 (0.74506)
		/	/	0.3136 (0.2756)	0.5840 (0.53664)

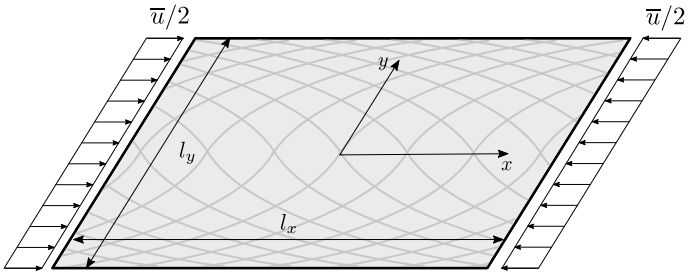

Figure 1: Variable stiffness plate: dimensions and reference system.

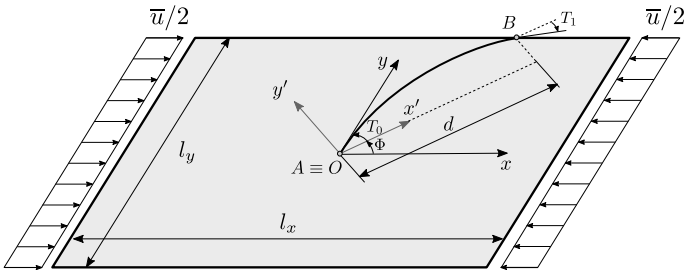

Figure 2: Definition of the fibers' orientation.

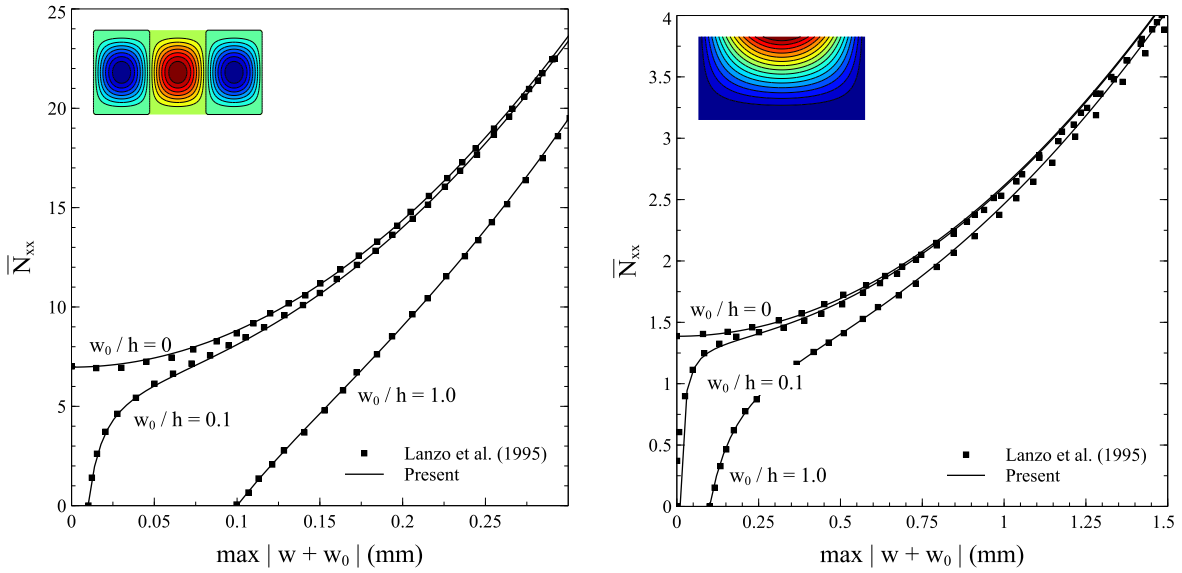

Figure 3: Isotropic plate with three levels of imperfection and subjected to prescribed axial force; aspect ratio r=2, and boundary conditions: (a) SCSC, (b) SFSC.

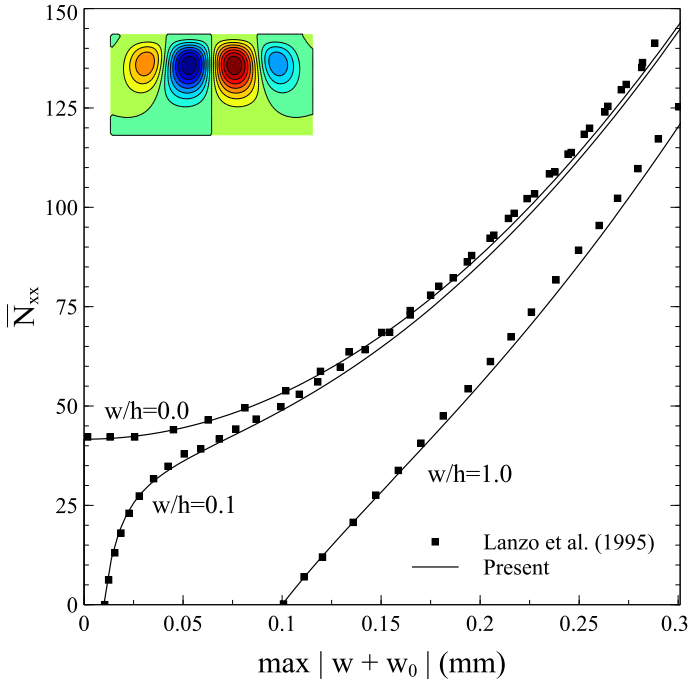

Figure 4: Isotropic plate with three levels of imperfection and subjected to prescribed in-plane bending; aspect ratio r=2, and CCCC boundary conditions.

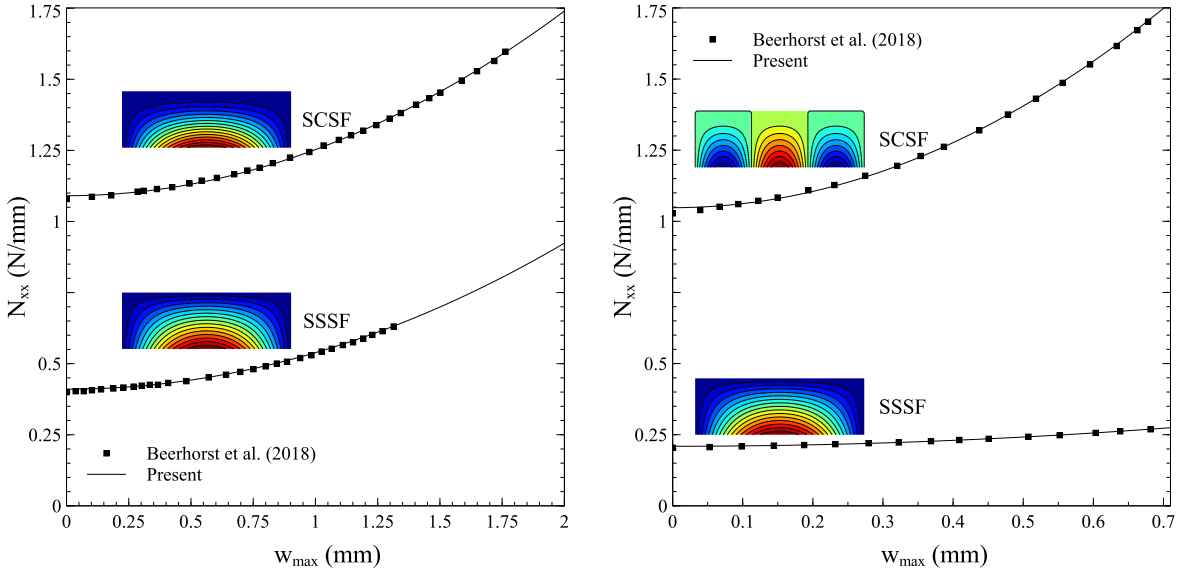

Figure 5: Axial force versus maximum out-of-plane displacement for cross-ply laminate with aspect ratio r=3 and lay-up: (a) $[0/90]_s$, (b) $[90/0]_s$.

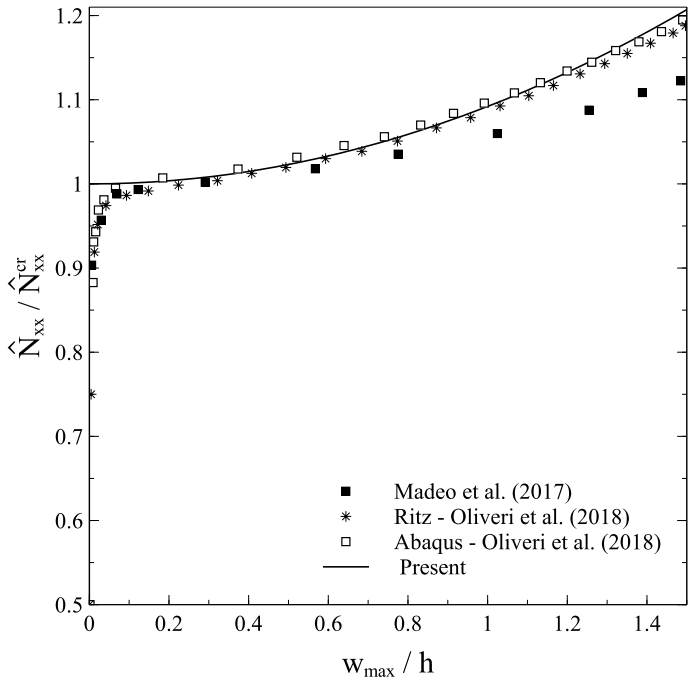

Figure 6: Axial force versus maximum out-of-plane displacement for variable-stiffness plate; aspect ratio r=1, and CCCC boundary conditions.

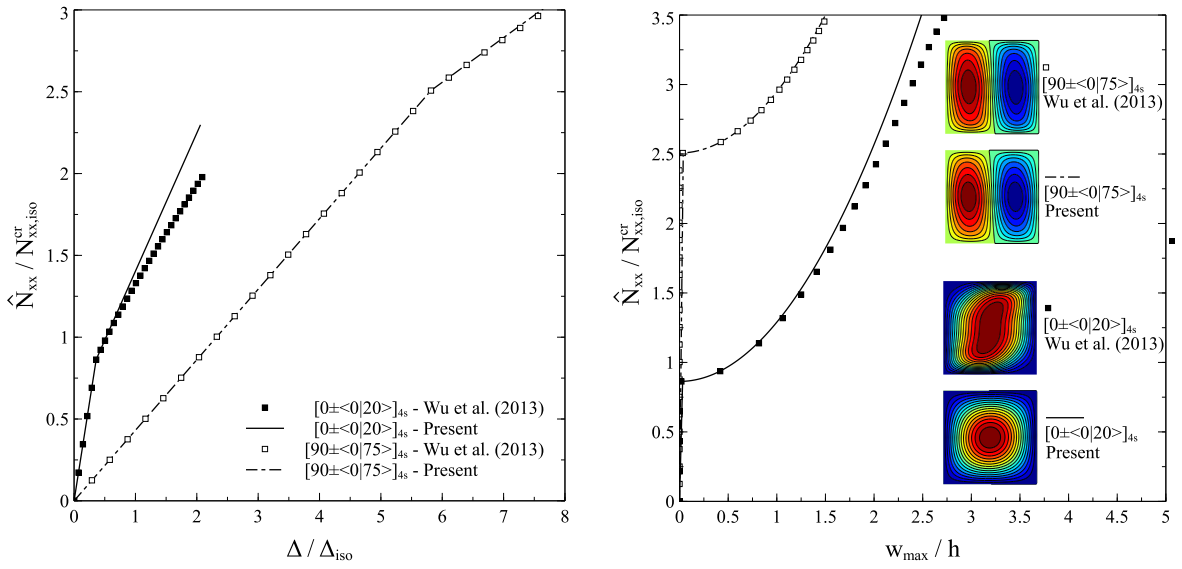

(a) (b)

Figure 7: Post-buckling response of variable-stiffness panels in terms of: (a) force versus axial shortening, (b) force versus maximum out-of-plane displacement (deflected patterns are reported at $\hat{N}_{xx}/N^{\mathrm{cr}}_{xx,\mathrm{iso}}$=3.5).

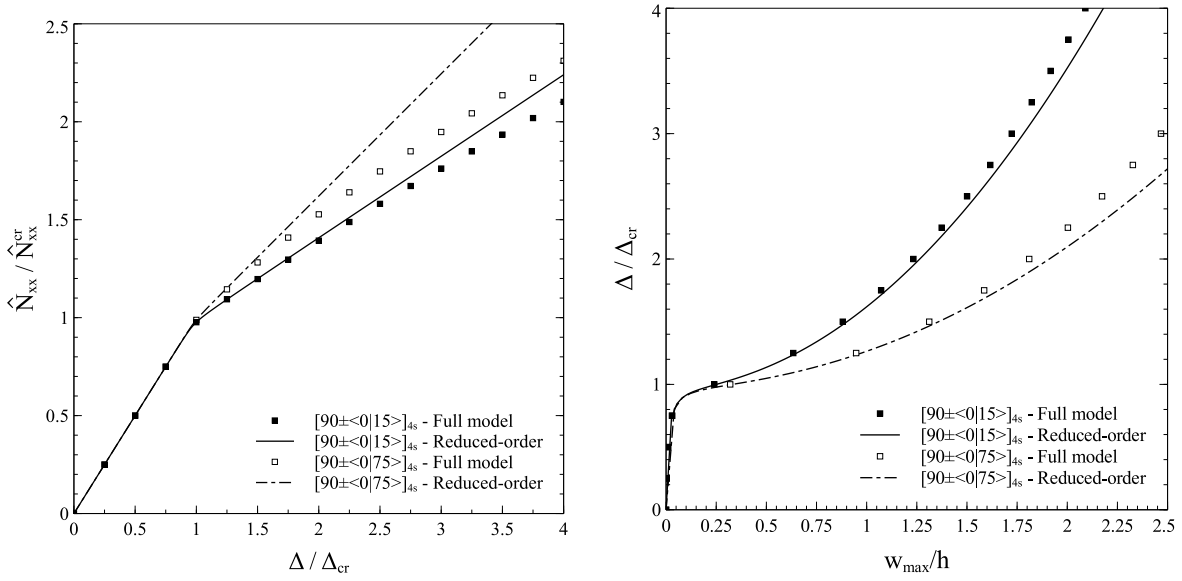

Figure 8: Post-buckling response of variable-stiffness panels ($[90\pm < T_0|T_1 >]_{4s}$, and $T_0 = 0$) using reduced-order and full model: (a) force versus axial shortening, (b) axial shortening versus maximum out-of-plane displacement.

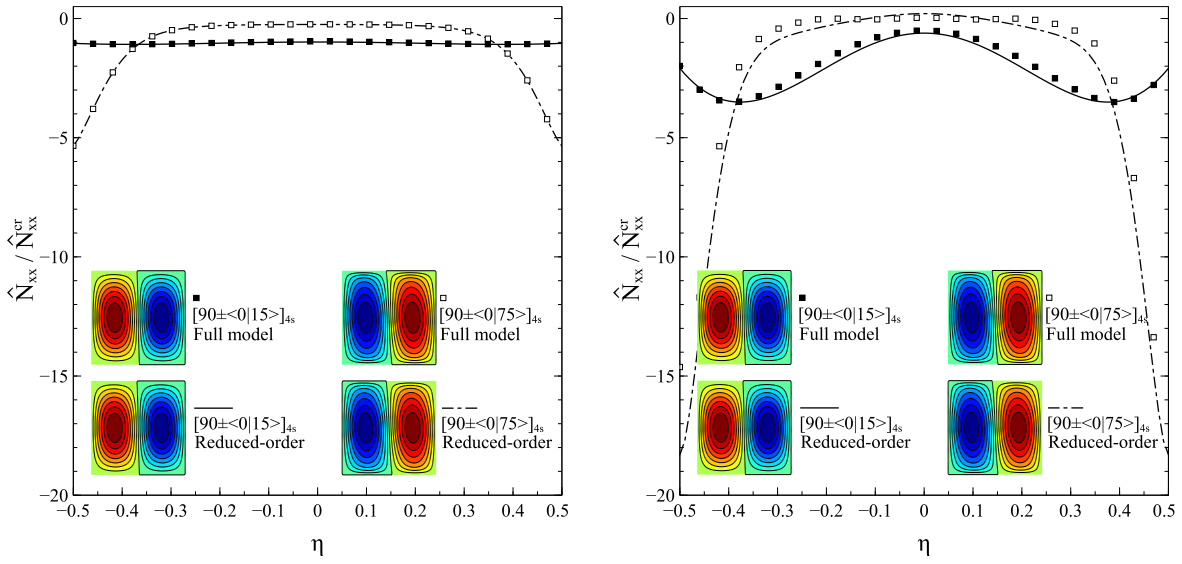

Figure 9: Post-buckling response of variable-stiffness panels ($[90\pm < T_0|T_1 >]_{4s}$, and $T_0 = 0$)using reduced-order and full model. Axial force at the loaded edge at: (a) $\Delta/\Delta_{cr} = 1.1$, (b) $\Delta/\Delta_{cr} = 4.0$.

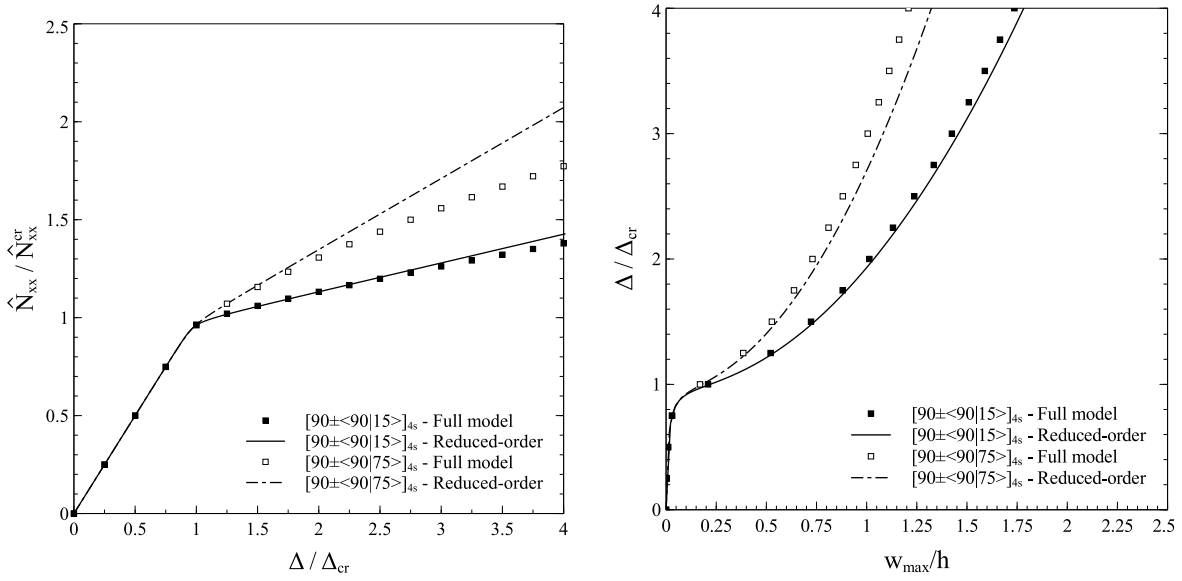

(a) (b)

Figure 10: Post-buckling response of variable-stiffness panels ($[90\pm < T_0|T_1 >]_{4s}$, and $T_0 = 90$ using reduced-order and full model: (a) force versus axial shortening, (b) axial shortening versus maximum out-of-plane displacement.

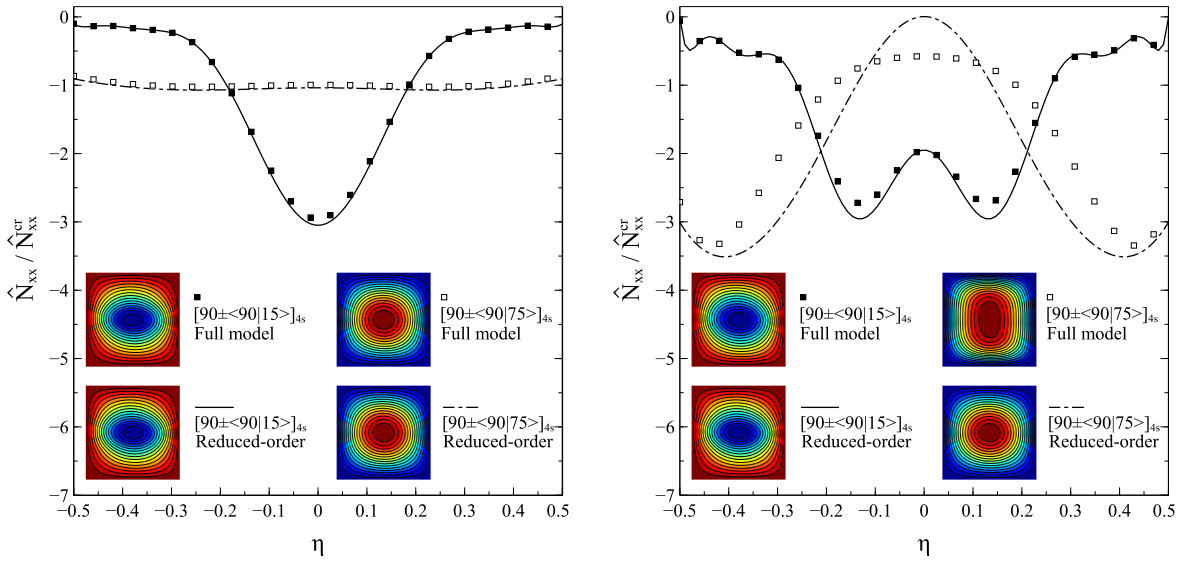

(a) (b)

Figure 11: Post-buckling response of variable-stiffness panels ($[90\pm < T_0|T_1 >]_{4s}$, and $T_0 = 90$) using reduced-order and full model. Axial force at the loaded edge at: (a) $\Delta/\Delta_{cr} = 1.1$, (b) $\Delta/\Delta_{cr} = 4.0$.

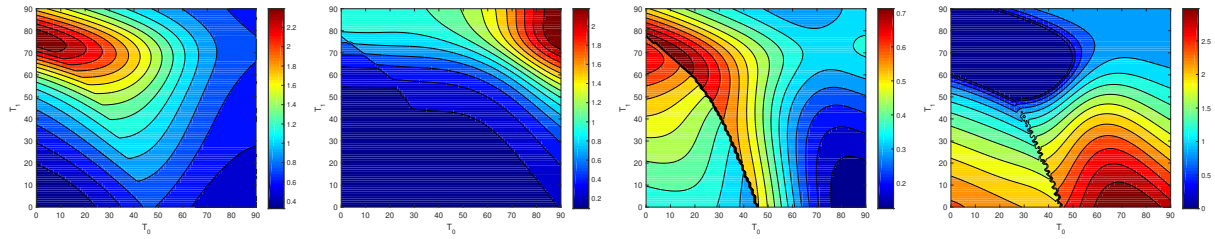

(a) (b) (c) (d)

Figure 12: Buckling and post-buckling response of axially compressed plates with lay-up $[90\pm < T_0|T_1 >]_{4s}$, $r = 1$ and SSSS: (a) $\hat{N}_{xx}^{\mathrm{cr}}/N_{xx,\mathrm{iso}}^{\mathrm{cr}}$, (b) $K_{\mathrm{pb}}/K_{\mathrm{pb,iso}}$, (c) K_{r}, (d) $w_{\mathrm{max}}/w_{\mathrm{max,iso}}$

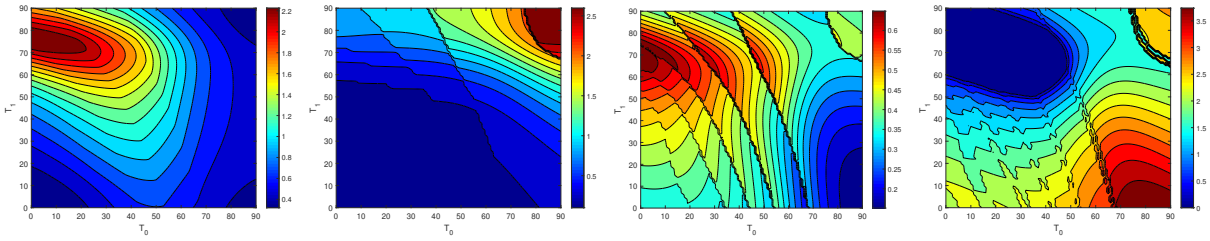

(a) (b) (c) (d)

Figure 13: Buckling and post-buckling response of axially compressed plates with lay-up $[90\pm < T_0|T_1 >]_{4s}$, $r = 3$ and SSSS constraints: (a) $\hat{N}_{xx}^{\mathrm{cr}}/N_{xx,\mathrm{iso}}^{\mathrm{cr}}$, (b) $K_{\mathrm{pb}}/K_{\mathrm{pb,iso}}$, (c) K_{r}, (d) $w_{\mathrm{max}}/w_{\mathrm{max,iso}}$

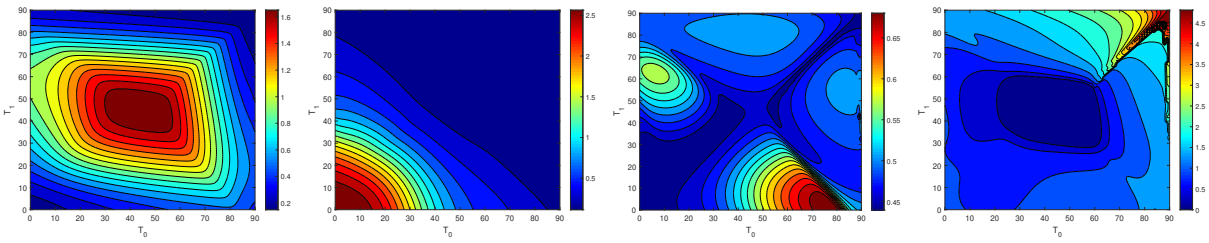

(a) (b) (c) (d)

Figure 14: Buckling and post-buckling response of axially compressed plates with lay-up $[0\pm < T_0|T_1 >]_{4s}$, $r = 10$ and SSSF constraints: (a) $\hat{N}^{\mathrm{cr}}_{xx}/N^{\mathrm{cr}}_{xx,\mathrm{iso}}$, (b) $K_{\mathrm{pb}}/K_{\mathrm{pb,iso}}$, (c) K_{r}, (d) $w_{\mathrm{max}}/w_{\mathrm{max,iso}}$

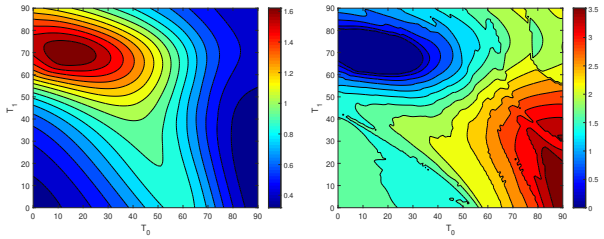

(a) (b)

Figure 15: Buckling and post-buckling response of plates subjected to in-plane bending, and with lay-up $[90\pm < T_0|T_1 >]_{4s}$, $r = 3$ and CCCC constraints: (a) $\hat{N}^{\rm cr}_{xx}/N^{\rm cr}_{xx,\rm iso}$, (b) $w_{\rm max}/w_{\rm max,iso}$

6 Appendix

A matrix is denoted as:

$$A_{(i)(j)} = \mathbf{A} \tag{37}$$

where the brackets identify the row and column indexes. This notation is useful for avoiding misinterpretations whenever the matrix is constructed starting from arrays of scalars with three or more indexes. For instance:

$$A_{(ik)(rs)} = \mathbf{A} \tag{38}$$

specifies a matrix where each couple of values ik defines a given row, whilst rs identifies the column index. Similarly, it is possible to consider arrays of matrices, such as $A_{(ik)(rs)(mn)}$. In this case, the following notation is adopted

$$\begin{aligned} \boldsymbol{\mathcal{A}}_{(ik)} &\longrightarrow \text{ array of the matrices } A_{(rs)(mn)} \\ \boldsymbol{\mathcal{A}}_{(rs)} &\longrightarrow \text{ array of the matrices } A_{(ik)(mn)} \\ \boldsymbol{\mathcal{A}}_{(mn)} &\longrightarrow \text{ array of the matrices } A_{(ik)(rs)} \end{aligned} \tag{39}$$

The absence of brackets will denote a vector.

The integrals entering Eqs. (18)-(21) are reported below. The prime denotes differentiation with respect to the variable ξ or η. No ambiguity exists due to the separation of variables operated in Eqs. (10) and (13)

$$S^{cc}_{(k)(\overline{k})} = \mathbf{S}^{cc} = -\int_{\overline{S}} r^4 a_{11} L_k L_{\overline{k}} \mathrm{d}\overline{S} \tag{40}$$

where $\overline{S} \equiv [-1,1] \times [-1,1]$.

$$\begin{aligned} S^{\Phi\Phi}_{(pq)(\overline{pq})} = \mathbf{S}^{\Phi\Phi} = \int_{\overline{S}} \big[& r^4 a_{11} F_p G''_q F_{\overline{p}} G''_{\overline{q}} + r^2 a_{12} \left(F''_p G_q F_{\overline{p}} G''_{\overline{q}} + F_p G''_q F''_{\overline{p}} G_{\overline{q}} \right) + a_{22} F''_p G_q F''_{\overline{p}} G_{\overline{q}} + \\ & + r^2 a_{66} F'_p G'_q F'_{\overline{p}} G'_{\overline{q}} - r^3 a_{16} \left(F_p G''_q F'_{\overline{p}} G'_{\overline{q}} + F'_p G'_q F_{\overline{p}} G''_{\overline{q}} \right) - r a_{26} \left(F''_p G_q F'_{\overline{p}} G'_{\overline{q}} + F'_p G'_q F''_{\overline{p}} G_{\overline{q}} \right) \big] \mathrm{d}\overline{S} \end{aligned} \tag{41}$$

$$\begin{aligned} K^{ww}_{(mn)(\overline{mn})} = \mathbf{K}^{ww} = \int_{\overline{S}} \big[& D_{11} X''_m Y_n X''_{\overline{m}} Y_{\overline{n}} + r^2 D_{12} \left(X''_m Y_n X_{\overline{m}} Y''_{\overline{n}} + X_m Y''_n X''_{\overline{m}} Y_{\overline{n}} \right) + \\ & + r^4 D_{22} X_m Y''_n X_{\overline{m}} Y''_{\overline{n}} + 4 r^2 D_{66} X'_m Y'_n X'_{\overline{m}} Y'_{\overline{n}} + \\ & + 2 r D_{16} \left(X''_m Y_n X'_{\overline{m}} Y'_{\overline{n}} + X'_m Y'_n X''_{\overline{m}} Y_{\overline{n}} \right) + 2 r^3 D_{26} \left(X_m Y''_n X'_{\overline{m}} Y'_{\overline{n}} + X'_m Y'_n X_{\overline{m}} Y''_{\overline{n}} \right) \big] \mathrm{d}\overline{S} \end{aligned} \tag{42}$$

$$S^{\Phi c}_{(pq)(k)} = \mathbf{S}^{\Phi c} = -\int_{\overline{S}} \left(r^4 a_{11} F_p G''_q L_k + r^2 a_{12} F''_p G_q L_k - r^3 a_{16} F'_p G'_q L_k \right) \mathrm{d}\overline{S} \tag{43}$$

$$\hat{\mathcal{N}}_{(k)(mn)(\overline{mn})} = r^2 \int_{\overline{S}} L_k X'_m Y_n X'_{\overline{m}} Y_{\overline{n}} \mathrm{d}\overline{S} \tag{44}$$

$$\begin{aligned}\mathcal{N}_{(pq)(mn)(\overline{mn})} = r^2 \int_{\overline{S}} \big[& F_p G''_q X'_m Y_n X'_{\overline{m}} Y_{\overline{n}} - \left(F'_p G'_q X'_m Y_n X_{\overline{m}} Y'_{\overline{n}} + F'_p G'_q X_m Y'_n X'_{\overline{m}} Y_{\overline{n}}\right) + \\ & + F''_p G_q X_m Y'_n X_{\overline{m}} Y'_{\overline{n}} \big] \, \mathrm{d}\overline{S}\end{aligned} \tag{45}$$

$$P_k^c = \mathbf{P}^c = \frac{ar^2}{2} \int_{-1}^{1} L_k \mathrm{d}\eta \, \overline{u} \tag{46}$$

$$N_k^c = \mathbf{N}^c = -\frac{2}{b^2} \int_{-1}^{1} L_k \mathrm{d}\eta \tag{47}$$